2015-12-01

# Characterizing the Effects of Capillary Flow During Liquid Composite Molding

Michael Ray Morgan
*Brigham Young University - Provo*

# Characterizing the Effects of Capillary Flow During Liquid Composite Molding

Michael Ray Morgan

A thesis submitted to the faculty of
Brigham Young University
in partial fulfillment of the requirements for the degree of

Master of Science

Andrew R. George, Chair
Michael P. Miles
David T. Fullwood

School of Technology

Brigham Young University

December 2015

ABSTRACT

Characterizing the Effects of Capillary Flow
During Liquid Composite Molding

Michael Ray Morgan
School of Technology, BYU
Master of Science

As the aerospace industry continues to incorporate composites into its aircraft, there will be a need for alternative solutions to the current autoclaving process. Liquid composite molding (LCM) has proven to be a promising alternative, producing parts at faster rates and reduced costs while retaining aerospace grade quality.

The most important factor of LCM is controlling the resin flow throughout the fiber reinforcement during infusion, as incomplete filling of fibers is a major quality issue as it results in dry spots or voids. Void formation occurs at the resin flow front due to competition between viscous forces and capillary pressure. The purpose of this work is to characterize capillary pressure in vacuum infusion, and develop a model that can be incorporated into flow simulation.

In all tests performed capillary pressure was always higher for the carbon fiber versus fiberglass samples. This is due to the increased fiber packing associated with the carbon fabric. As the fabric samples were compressed to achieve specific fiber volumes an increase in capillary pressure was observed due to the decrease in porosity. Measured values for capillary pressure in the carbon fabric were ~2 kPa, thus the relative effects of $P_{cap}$ may become significant in flow modeling under certain slow flow conditions in composite processing.

Keywords: capillary pressure, liquid composite molding, vacuum infusion, carbon fiber, resin infusion

# ACKNOWLEDGEMENTS

I would like to express my gratitude and appreciation to Dr. Andrew George for the constant encouragement and assistance during the course of this research. His enthusiasm and vision for the future of composite processing was a motivating force for the completion of this work.

Mention is made to my fellow classmate and colleague, Paul Hannibal, whose research aided in the analysis and results of this work.

Love and appreciation to my wife Emily, for her constant support, patience, and sacrifice through out this experience. Also to my parents, siblings, and friends who took interest in my work and provided help and advice when needed.

TABLE OF CONTENTS

**LIST OF FIGURES** ..... **vi**

**1 Introduction** ..... **1**

1.1 Composite Incorporation and Purpose ..... 2

1.1.1 Economical Benefits and Environmental Goals ..... 4

1.2 Manufacturing Processes ..... 5

1.2.1 Autoclave Processing ..... 5

1.2.2 Out-of-Autoclave (OoA) Processing ..... 6

1.2.3 Liquid Composite Molding (LCM) ..... 6

1.3 Simulation Modeling ..... 7

1.4 Problem Statement ..... 9

1.5 Hypotheses ..... 9

**2 Literature Review** ..... **10**

2.1 Capillary Pressure Measurement Methods ..... 12

2.2 Modeling Capillary Pressure ..... 15

**3 Methodology** ..... **18**

3.1 Fabric ..... 18

3.2 Test Fluid ..... 18

3.3 Experimental Design ..... 19

3.3.1 Fabric Dip Tests ..... 19

3.3.2 DIC/DAQ Vacuum-Bag Infusions ..... 21

**4 Research Results and Analysis** ..... **24**

4.1 Fabric Dip Tests ..... 24

4.1.1 Height vs. Time Data Acquisition ..... 24

4.1.2 Capillary Pressure Calculation Methods ..... 26

4.1.2.1 Method A – Neglecting Gravity ..... 26
4.1.2.2 Method B – Partially Accounting for Gravity ..... 28
4.1.2.3 Method C – Fully Accounting for Gravity ..... 29
4.1.3 Uncompressed Dip Test $P_{cap}$ Results ..... 30
4.1.4 Compressed Dip Test $P_{cap}$ Results ..... 36
4.1.5 Comparison of $P_{cap}$ Results with Prediction ..... 42
4.2 DIC/DAQ Infusion Results ..... 45
4.2.1 Permeability Determination ..... 45
4.2.1.1 Fiberglass Permeability ..... 45
4.2.1.2 Carbon Permeability ..... 47
4.2.2 Comparison of Compressibility for Infusion and Squeeze-flow ..... 49
4.2.3 Pressure Gradient Comparison ..... 50
4.3 $P_{cap}$ Comparison Between Dip Tests and DIC/DAQ Testing ..... 55
**5 Conclusions ..... 57**
5.1 Future Recommendations ..... 58
**REFERENCES ..... 59**

LIST OF FIGURES

Figure 1-1: Pictorial Representation of Materials Used on the Boeing 787 Dreamliner ..... 3

Figure 3-1: Vectorply Carbon Fiber (left) and JB Martin Fiberglass (right) Samples ..... 18

Figure 3-2: Experimental Setup for Compressed Fabric Dip Tests ..... 21

Figure 3-3: DIC/DAQ Test Plate Drawing ..... 22

Figure 3-4: Experimental Setup of DIC/DAQ System ..... 23

Figure 4-1: Partially Saturated Carbon Fiber (Left) and Fiberglass (Right) Fabrics ..... 24

Figure 4-2: Flow Front Advancement in Carbon Fiber at 5, 20, and 50 Minutes ..... 25

Figure 4-3: Original and Binary Image of Saturated Samples ..... 26

Figure 4-4: $h^2$ vs. $t$ Average Profiles for Uncompressed Dip Tests ..... 31

Figure 4-5: Uncompressed $P_{cap}$ Results for Method A: Each Sample (top); Averaged by Orientation (bottom) ..... 32

Figure 4-6: Uncompressed $P_{cap}$ Results for Method B: Each Sample (top); Averaged by Orientation (bottom) ..... 33

Figure 4-7: Uncompressed Method C Plots for Determination of Average $P_{cap}$: Carbon (top), Fiberglass (bottom) ..... 34

Figure 4-8: Average $P_{cap}$ Values for Uncompressed Flow Tests ..... 36

Figure 4-9: $h^2$ vs. $t$ Average Profiles for Compressed Dip Tests: Carbon (left), Fiberglass (right) ..... 37

Figure 4-10: Linear Fits for Only First Few Data Points from Figure 4-9 ..... 38

Figure 4-11: Compressed $P_{cap}$ Results for Method A: Carbon (left), Fiberglass (right); Individual (top), Averaged (bottom) ..... 39

Figure 4-12: Compressed $P_{cap}$ Results for Method B: Carbon (left), Fiberglass (right); Individual (top), Averaged (bottom). ..... 40

Figure 4-13: Compressed Method C Plots for Determination of Average $P_{cap}$: Carbon (top), Fiberglass (bottom) ..... 41

Figure 4-14: Average $P_{cap}$ Values Throughout a Compressed Flow Test ..... 42

Figure 4-15: Fabric Compressibility Measurement Results from DIC/DAQ Testing for Fiberglass Infusion 2 and 3 ..... 46

Figure 4-16: Permeability as a Function of Fiber Content, Fit to Infusion Data, for Fiberglass DIC/DAQ Infusions..... 47

Figure 4-17: Compressibility Measured from Hannibal (2015) for Carbon Reinforcement..... 48

Figure 4-18: Permeability as a Function of Fiber Content Fit to Infusion Data..... 48

Figure 4-19: Compressibility Determined by Instron During Squeeze Flow and by DIC/DAQ During Vacuum Infusion..... 50

Figure 4-20: Inferred Pressure Gradient Results (George 2011)..... 51

Figure 4-21: Experimental and Simulated Resin Pressure Gradient from Inlet to Flow Front for Carbon-3 DIC Infusion..... 53

Figure 4-22: Experimental and Simulated Data of $P_R$ gradient..... 56

# 1 INTRODUCTION

Over the past decade civil aerospace manufacturers have made incredible technological advancements with the incorporation of composite materials into their private and commercial airplanes. The replacement of metal components by advanced composites has provided many advantages and allowed for a lighter, more fuel-efficient aircraft. As industry continues to realize the advantages of composite materials, it is continually searching for alternate solutions to the current cumbersome manufacturing methods. Liquid composite molding (LCM) has proven to be a promising alternative, producing parts at faster rates and reduced costs while retaining aerospace grade quality.

The most important factor of LCM is controlling the resin flow throughout the fiber reinforcement during infusion. Incomplete filling of fibers is a major quality issue as it results in dry spots or voids, consequently decreasing the mechanical properties of the part. Simulation software has been developed to better understand resin flow of different resin/fiber combinations in an effort to improve mold design and eliminate void formation. Current simulation software has limited accuracy when applied to particular processes due to inadequacies in addressing capillary pressure.

Capillary pressure, also known as "wicking," is the ability of a liquid to flow in narrow spaces without the assistance of, and in opposition to external forces like gravity. During resin infusion (RI), capillary pressure allows fiber bundles (tows or roving) to absorb resin until

complete saturation of the fiber bundle is achieved. This phenomenon has typically been deemed negligible in simulation due to the use of high infusion pressures or low fiber content materials during infusion processes. However, as incorporation of LCM processes into the commercial aerospace industry is accepted for high-performance and large structural parts, high fiber content materials along with low pressures (vacuum only for large parts) are required, causing capillary pressures to be a significant component in accurate simulations of resin flow.

## 1.1 Composite Incorporation and Purpose

The aerospace industry for nearly a century has relied on metals for the structural support and skin of its airplanes. This began in 1915 with the Junker J1, the first all metal airplane, composed of an age hardened aluminum alloy known as duralumin. As airplane design continued to advance, so did the metals with which they were built. Exotic aluminum alloys were developed to meet specific needs, along with the incorporation of hard metals such as stainless steels, nickel alloys, and titanium. Integrating these metals into critical areas of the body, wings, and engines has enabled aerospace manufacturers to design and produce aircraft ranging from supersonic fighter jets to double-deck, wide bodied airliners. Though metal has and will continue to play a critical role in airplane design, industry has turned to alternative materials such as advanced composites to provide comparable properties with less weight.

Application of composites on civil airplanes began with the interior cabin of the Boeing 707. Fiberglass composite was used on detail components within the cabin totaling a mere two percent of the structural weight. Since the 707, both Boeing and Airbus have increased the use of composites in their commercial airplanes as knowledge and manufacturability of composites have improved.

In 2005 Airbus debuted the A380 utilizing composites extensively in the wings, tail section, fuselage undercarriage, and doors. The A380 was also the first commercial airplane to have a central torsion box made of carbon fiber reinforced plastic (CFRP). The sum of the composites used on the A380 totaled 25 percent of the structural weight. Four years later Boeing announced the 787 Dreamliner, which has composites comprising 50 percent of the structural weight as shown in Figure 1-1 (Boeing 787 Dreamliner Specs 2015). It was the first commercial aircraft to use CFRP extensively on both the skin and structure of the fuselage. In 2016 it is projected for the Airbus A350 to hit the market and will surpass the 787 in overall composite use. Just like the 787 its fuselage skin and structure will be composed of composites totaling more than 53 percent of the structural weight. These airplanes represent the commercial sector's ingenuity and innovation to achieve both economical benefits and environmental goals.

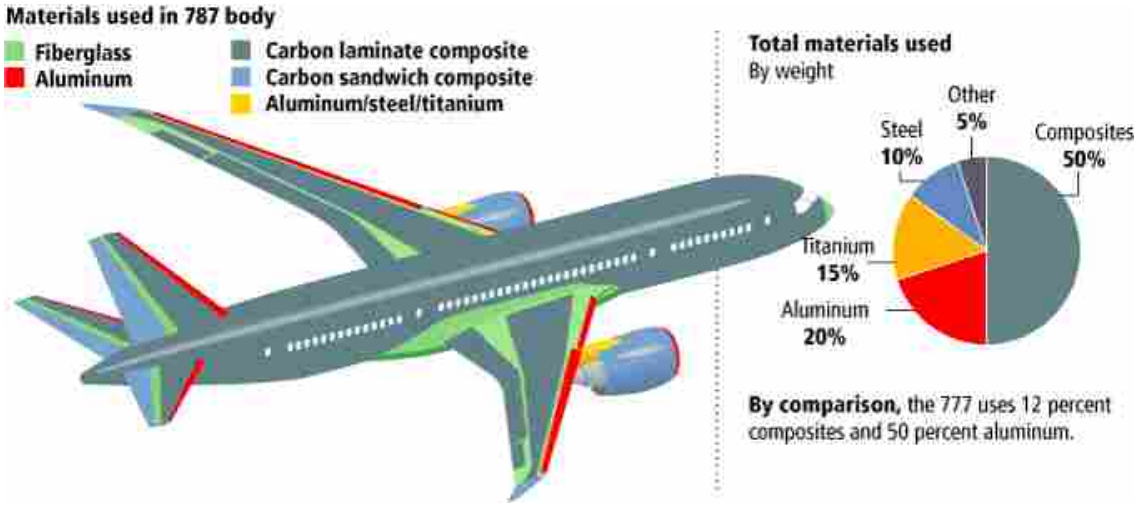


**Figure 1-1: Pictorial Representation of Materials Used on the Boeing 787 Dreamliner**

### 1.1.1 Economical Benefits and Environmental Goals

Financial savings that are realized through the application of composites materials are attributed to their net-shape capabilities, mechanical and chemical properties, and overall weight reduction. Composite parts are constructed from layers of carbon fabric molded within a resin matrix into a net shape, eliminating almost all scrap material. This is completely opposite from metal parts which are typically cut from a block, forging, or casting, resulting in immediate loss in material costs due to metal removal.

Mechanical and chemical properties of composites are also very beneficial financially. Benefits such as increased strength, superior durability, and corrosion resistance, has allowed for reduced maintenance costs and service inspections. On the Airbus A350, the service intervals have been reduced from 6 years to 12, which significantly reduced maintenance costs for customers (Innovative Materials 2015).

The largest financial impact, particularly in the long term, is reducing fuel consumption. This is achieved by reducing the overall weight of the airplane. Composites materials are typically 20 percent lighter than aluminum allowing manufacturers to maximize weight reduction. This is a substantial savings on planes such as the 787 and A350 when considering that over 50 percent of the structural weight is composite.

Reduced fuel consumption is not only economically- but also environmentally- friendly. It is helping to further reach the goals that the Advisory Council for Aviation Research and Innovation in Europe (ACARE) had in their 2001 report "European Aeronautics: A Vision for 2020" (Argüelles 2001). In the report's environmental section it asked for there to be a total engagement by the industry in a task of studying and minimizing the industry's impact on the global environment with 3 major goals outlined:

1. A reduction in perceived noise to one half of the current average levels.

2. A 50% cut in CO2 emissions per passenger kilometer (which means a 50% cut in fuel consumption in the new aircraft of 2020)

3. An 80% cut in nitrogen oxide (NOx) emissions.

## 1.2 Manufacturing Processes

Processing of aerospace grade composite has two main requirements; one is minimal void content, second being high fiber content of around 60 percent. Achieving both these requirements maximizes the mechanical properties of the fiber/resin combination, while minimizing weight. The most commonly used and reliable method to meet these requirements is autoclave processing. Though reliable, autoclaves have their drawback such as high operating costs and batch processing. This is why industry is actively pursuing the development of out-of-autoclave processing that can meet quality requirements in order to reduce costs and increase efficiency. LCM has been proven to be able to achieve both minimal void content along with high fiber content.

### 1.2.1 Autoclave Processing

Autoclave processing utilizes pre-impregnated (pre-preg) fibers along with high pressure to aid in complete wet out and high fiber content. Pre-preg fibers come in different forms, such as unidirectional fiber rolls or woven mats, allowing for the layup process to be performed by hand or automation. Fibers are applied to the mold in a designed layered pattern to apply stiffness and strength to specific features of the part. The part may go through several debulking cycles in order to remove air between layers and increase fiber density. A final vacuum bagging is applied to the part, and it is placed in the autoclave oven. A vacuum hose will remain

connected to the part, while the oven is brought up to temperature and pressure. As temperature increases it begins to cure the resin and pressure helps to remove excess resin along with increasing the adhesion between fiber layers.

Drawbacks to the autoclaving process involve both cost and efficiency. The autoclave itself is a substantial capital investment, especially as the size of the part increases. High operational costs are associated with the energy required to reach both temperature and pressure during curing. Curing cycles limit production to batch processing which reduces the rate and efficiency at which the parts can be produced. As demand for aerospace composite structures increases, it could easily surpass the autoclave capacity that is currently available in industry.

### 1.2.2 Out-of-Autoclave (OoA) Processing

Out-of-autoclave manufacturing techniques are alternatives to the current high-pressure autoclave process. Typically OoA is very similar to the traditional autoclave process; utilizing pre-preg fibers consolidated under a vacuum bag, but as the name implies it is simply oven cured versus using an autoclave. These OoA prepregs are designed with lower viscosity resins to achieve similar consolidation and degassing of voids at lower pressures. There are other techniques that have been developed such as liquid composite molding, which utilizes dry fibers that are infused with resin, then oven cured.

### 1.2.3 Liquid Composite Molding (LCM)

Liquid composite molding is a family of processes that utilize either double sided molds, or single sided mold with vacuum bag. Determined by the mold and process used, resin is forced through the fibers using mechanical pressure, vacuum pressure, or a combination of the two. These processes have been shown to be very reliable and cost effective at producing comparable

parts to autoclave qualities. Resin transfer molding (RTM) has been successfully proven to produce aerospace grade quality parts with minimal void content, and high fiber contents. One of the drawbacks to RTM is because of high infusion pressures, a double-sided mold is required, reducing its cost effectiveness for large composite parts. A solution is the advancement of a current process known as vacuum infusion (VI).

Vacuum infusion requires only a single sided mold, covered in vacuum bagging. Similar to autoclave processing, air is completely evacuated from the layup, minimizing entrapped air and compressing the fibers. Resin is then drawn through the fibers until complete saturation is achieved. Additional steps such as bleed out and vacuum at the inlet for less thickness variation may be performed for optimal properties before parts are placed in the oven for curing.
The main limitation of LCM processes and particularly VI is the comprehension and control of the resin flow front during infusion. Unlike random fiber mats, engineered woven fabric mats display dual scale flow during resin saturation. This is due to the macro flow that occurs between fiber tows, and micro-flow occurring as individual fibers become saturated within the tows. Different effects are observed during infusions involving high pressure, low pressures, and different fiber/resin combinations. Simulation modeling has been developed to help overcome these parameters, but is not completely accurate for all processes.

### 1.3 Simulation Modeling

Simulation software including PAM-RTM, Polyworx, and LIMS has been developed to model resin flow during infusion processes. Modeling has aided in reducing both time and cost on mold development, which was traditionally accomplished through the trial and error method. Features such as inlets, vents, and outlet ports can be properly positioned within the software

before tooling is even created; reducing mold rework, and minimizing dry spots, voids, and race-tracking.

A current issue with simulation modeling is accurately modeling the resin flow front due to the limited knowledge of particular variables. One of these variables is the capillary pressure that is involved in the pressure gradient. Most modeling has neglected capillary pressure because of the nature of the two principle markets where flow simulation is used. For high-volume, smaller geometry composites, manufacturers use a resin transfer molding (RTM) type process, where high pressures are required to force resin through tightly packed fibers causing capillary pressures to be insignificant in comparison to the applied pressure gradient. In contrast, the marine/energy industry manufactures low-volume, large parts using VI with low fiber contents, decreasing the capillary effect that can occur between fibers. The aerospace industry will require a mixture of these two processing techniques over the next 20 years allowing for quick processes to produce large composite primary structures with high fiber content. Focus has been given to VI due to the fact that RTM is limited to the size of components that can be created because larger parts require pressures that are unfeasible.

In all cases, the accuracy of flow simulation is also hindered by the understanding of variables more significant than the capillary pressure, such as permeability. But flow simulation is constantly improving and capillary pressure is an issue that needs to be addressed. Critical issues that are dependent on capillary flow, such as void prediction, are becoming more prevalent in the literature. By neglecting capillary pressure, simulation models will be limited to the accuracy with which they can predict the resin flow rate and pattern. The purpose of this research is to characterize the capillary pressure effects in vacuum infusion, resulting in a model for capillary pressure that can be incorporated into flow simulation.

## 1.4 Problem Statement

Efforts have been made to model the VI process, but most have deemed capillary pressures insignificant because of low fiber volumes and high filling rates. By neglecting capillary pressure, simulation models will be limited to the accuracy with which they can predict the flow rate and pattern of a fiber resin combination in 3-dimensional modeling. The purpose of this research is to characterize the capillary pressure effects in vacuum infusion, resulting in a model for capillary pressure that can be incorporated into flow simulation.

## 1.5 Hypotheses

Capillary pressures will have a significant effect on the flow velocity when using high fiber content reinforcement and slow resin infusion. Incorporating this additional pressure into the pressure gradient will allow reasonable predictions of flow rates in both rigid tooling and vacuum infusions.

# 2 LITERATURE REVIEW

During RI the overall quality of parts produced is highly dependent on complete saturation of fibers by the resin flow front. As the resin flow front progresses throughout the fiber matrix there is the inherent risk of dry spots or voids forming, which have a detrimental effect on the physical and mechanical properties of the part. Research and studies have been conducted on resin flow to improve current simulation software and aid in the understanding and improvement of RI processes.

Complete saturation of a fiber preform requires all empty spaces between the fibers to be filled with resin, including the space between fiber tows and the spaces between each individual fiber that makes up the tow (Simacek 2010). Due to the complex architecture of engineered fabrics and the inherent variation of layup technique and processing methods, there is a probability that there will be regions inside fiber tows or in between fiber tows that will be devoid of resin. In Kuentzer's research (Kuentzer 2007) they hypothesized that pores within the tows take 4.5 times longer to fill than the regions between the fiber tows. This is related to the dual scale flow that has been observed at the resin flow front, which is the leading cause of void formation in RI processes.

Dual scale flow is caused by viscous forces around the fiber bundles (macroflow) and capillary forces between the fibers in the bundles (microflow) occurring simultaneously (Gourichon 2006). The competition of these two flows causes a large difference in the position

of the flow front leading to the potential of void formation (Chang 1997). In the case of a high resin velocity, voids will form within fiber tows because flow in the channel between tows is faster than in the tow because of the high permeability of the channel (Figure 2-1 b). For low resin velocity, however, the capillary flow will dominate within tows and hence voids will form in the channels between tows (Figure 2-1 a) (Patel 1996, Kang 2000). This interplay between the flows at the macro and micro scale will dictate whether the final microstructure of the composite part manufactured is devoid of dry spots and voids.

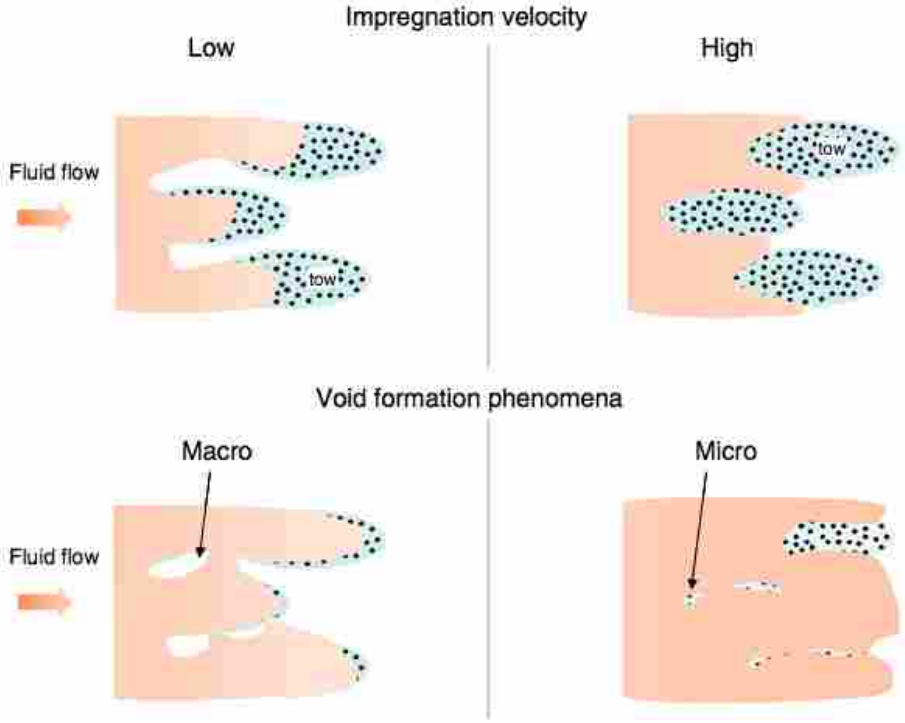


**Figure 2-1: Macro and Micro Void Formation. Reprinted from LeBel (2014)**

Void content within a composite part is considered as representative of the part's structural integrity. As the presence of voids increases there is a degenerate effect on mechanical performances such as interlaminar shear strength, flexural strength and compressive strength (Ruiz 2006). Minimal void content is required in aerospace applications, and as the content

increases, so does the risk or scrapping the part. Therefore, in order to avoid the creation of voids in the composite part, it is critical to understand not only the flow behavior at the macro scale, but also what the role of capillary effects is in micro-impregnating the porous network.

Simulation of resin infusion is based on measurement or calculation of the pressure gradient; the flow velocity is directly proportional to that pressure gradient. $P_{cap}$ has been shown to affect that pressure gradient (Lai 1997, Ahn 1991), although little effort to couple $P_{cap}$ to filling simulation exists in literature (Section 2.2), and even less to experimentally validate any $P_{cap}$ -coupled filling simulation model. At low pressure conditions in RI such as during slower resin velocity when the flow front is far from the inlet, the levels of $P_{cap}$ that have been measured in literature can exceed the mechanically applied pressure gradient, thus implying that flow simulation would be much more accurate when accounting for capillary effects.

## 2.1 Capillary Pressure Measurement Methods

Different measurement methods have been used to determine the capillary pressure in fluid saturation of carbon and fiberglass fibers. A common first step to understanding capillary forces is measurement of the wicking behavior of the fluid, based on the Wilhelmy plate method, a test designed to calculate the surface tension of a liquid by measuring the force acted on a vertically immersed plate. The surface tension of a liquid may be considered one of the most important parameters influencing resin impregnation, as is it plays a key role in determining the wettability of reinforcing fibers by a resin matrix in composite processing. Related to the surface tension, is the contact angle, which decreases with the surface tension of the liquid. As the contact angle decreases, the wettability of the system is said to improve. This has been found to translate in to

larger capillary pressures, which produce a higher rate of liquid penetration into fiber bundles by wicking flow (Lee 1988, Ahn 1991).

Lee (1988) used this principle when performing dynamic wettability measurements on carbon and Teflon fibers immersed in silicone oil and epoxy resin. A single fiber was immersed in the liquids and the surface tension and contact angle was calculated for each interaction. This work showed that the dynamic fiber wettability measurements give direct information on the interaction between the fiber and resin to be processed.

Batch *et al* (1996) also applied Wilhelmy's principle when measuring capillary flow, driven by capillary forces only, in longitudinal and transverse direction inside fiber bundles. The saturation rate was measured by suspending a fiber filled tube and submersing the base into a fluid. As the fluid penetrated the fiber the increase of weight could be observed. This work was unique as the fiber was held within a glass tube, which could influence the capillary flow of the liquid.

Ahn *et al* (1991) designed and constructed an apparatus capable of measuring simultaneously the unsteady-state permeability and capillary pressure in a simulated composite impregnation experiment. Thirty plies of plain woven carbon fiber fabric were placed within the apparatus and resin was forced through the preform with a constant force. The experiments showed that as porosity increased capillary pressures decreased. At low porosity a maximum capillary pressure of 37 kPa was observed. This pressure value is significant compared to even the highest pressure gradient achievable in vacuum infusion, 100 kPa at sea level; a change of 37 kPa in the applied pressure gradient would result in a 37% change in the filling velocity for this case.

Patel and Lee (1996) used a centrifuge apparatus to measure capillary pressure-saturation relationships. The sample fiber mat was completely saturated with the test liquid and subjected to centrifugal force at various speeds of rotation. Centrifugal force tries to force the liquid out of the sample, while capillary pressure tries to contain it in the sample. The study also demonstrated that lower fiber reinforcement porosity results in higher capillary pressures, but reduces permeability and thus the bulk flow rate. Thus there would be an optimum porosity at which the spontaneous impregnation rates are the highest.

Amico (2000) performed two different capillary infiltration experiments. The first was similar to Lee (1988) and Batch *et al* (1996) where a single fiber was partially immersed in the wetting liquid, and as the liquid uptake occurred due to capillary pressures only, weight and height readings of the column of liquid were continuously taken. The second experiment performed was with the same device, but instead of a single yarn, a single layer of plain woven glass fabric was used, and height measurements were taken during the infiltration.

Neacsu (2006) studied radial impregnation of fiber tows. The cylindrical fibrous sample were created by wrapping glass fibers around a tube to thicknesses of 12.5-60 mm. Sensors were strategically inserted from one to five locations to signal arrival time of liquid saturation. The top and bottom of the fibers were sealed so liquid could only enter from the outside diameter and air could escape through the tube. The experiments were then initiated by immersing the sample in a bath of impregnating liquid.

Min Li (2010) performed two separate infusion experiments, the first being driven by vacuum pressures, the second driven by compressed air pressure. The employed driving pressure was sufficiently low, less than 60 kPa, so that capillary pressure effects could not be neglected. In these experiments the unidirectional glass fiber bundles were tested at different fiber volume

fractions of 50%, 60%, and 70%. Capillary pressures were then extrapolated from the data gathered from infusion experiments.

Lebel (2014) utilized capillary rise experiments similar to those performed in Amico (2000). The setup was developed to monitor simultaneously the flow front position and the total uptake mass by spontaneous imbibition during a 24 hour test. The fabric was held in a glass mold as it was lowered into a fluorescent dyed fluid. The dye, illuminated by a black light, allowed for visual tracking of the fluid as it saturated the glass fibers. In conjunction with digital images taken of the fluid rise, an automated tracking of the capillary front was developed in Matlab. The experimental methodology proposed in Lebel's paper can be used to characterize the imbibition properties of fiber tows and fabrics as well as penetrativity of thermosetting resins. Moreover, it can be used to identify the window of optimal flow front velocity to reduce void formation. The experiments performed in this paper are very similar to experiments carried out in this work and will be discussed later (section 3.3.1).

Note that only one previous test method characterized carbon fabrics (Ahn 1991), despite the fact that the lower porosity inherent in carbon reinforcements compared to glass should cause higher capillary pressures. This is assumed to be due to the opacity of carbon – which makes it more difficult to monitor fluid wetting of the fabric compared with fiberglass. This study aims to help fill in the gap of capillary characterization for carbon fabrics, where that data is needed the most.

## 2.2 Modeling Capillary Pressure

The modeling of capillary pressure has been applied in several different methods. Pillai (1998) modeled delayed impregnation of fiber tows by the inclusion of a "sink" (negative source

term) in the equation of continuity for the flow in the inter-two regions. Slade (2001) also characterized the unsaturated flow behavior of various mats using a constant sink term in a continuity equation, along with identifying a dimensionless number called the sink effect index $\psi$. The sink effect index characterizes the magnitude of liquid absorption by the tows and is a function of the relative resistance to the flow in the tow and inter-tow regions, and the packing density of the tows. Gourichon (2006) included a sink term in there modeling that represented liquid absorption velocity per unit volume and added additional volumes in the form of 1D elements in their simulation model.

A simpler method to model the effects of capillary pressure in resin flow is to modify the measured or calculated pressure gradient by adding (1991 Ahn) or subtracting (1997 Lai) the capillary pressure, depending on whether the capillary flow is faster or slower, respectively, than the bulk macro flow. As the flowrate during infusion is proportional to the pressure gradient, the changes due to the capillary pressure directly affect the flowrate.

Another method for accounting for capillary flow is through the capillary number *Ca*. The capillary number is a ratio of the viscous force to the capillary force and is define as:

$$Ca = \frac{\mu v}{\gamma} \tag{2-1}$$

where $\mu$ is the resin viscosity, $v$ is the global (macroscopic) resin velocity, and $\gamma$ is the surface tension of the resin. A modified capillary number was also sometimes used defined as:

$$Ca^* = \frac{\mu v}{\gamma cos\theta} \tag{2-2}$$

which included $\theta$ to account from the contact angle between the fiber and resin. The capillary number has often been used in permeability measurements (Hattabi 2005, Min Li 2010) and void

prediction models (Kang 2000, Gourichon 2006, Ruiz 2006) as void content could be shown to be a function of the capillary number.

# 3 METHODOLOGY

## 3.1 Fabric

Two types of fabric reinforcements were selected to evaluate the capillary pressures during saturation (Figure 3-1). The fiberglass reinforcement is an unbalanced weave, JB Martin TG-15-N (518 g/m$^2$) with PPG rovings. The carbon fiber sample is a +45/-45 biaxial non-crimped fabric (NCF), VectorPly C-BX 1800 (580 g/m$^2$).

**Figure 3-1: Vectorply Carbon Fiber (left) and JB Martin Fiberglass (right) Samples**

## 3.2 Test Fluid

The selected test fluid was store bought canola oil. This was an inexpensive alternative to resins and other chemicals while still providing comparable characteristics. The hydrocarbon-

polymer nature of canola oil results in similar fluid properties to an epoxy or polyester resin, e.g. surface tension, viscosity at room temperature, contact angles on a given surface.

## 3.3 Experimental Design

### 3.3.1 Fabric Dip Tests

Fabric samples were cut in 50 mm x 60 mm rectangles in both the warp and weft directions. This allowed enough fabric for mounting and immersion into the fluid, while maintaining a 50x50 $mm^2$ area of saturation. Other studies discussed using die cutting for samples to maintain edge quality, but a straight edge and razor were used with acceptable results as no significant shear or fabric damage were observed.

Fabric dip tests were performed in a black room held at a temperature of 20°C ± 2°C. Images were visually aided by a 75-watt fluorescent black light bulb and captured with a Sony Alpha DSLR camera equipped with a Sigma 50 mm f/2.8 EX DG macro lens. The fabric was slowly lowered until a minimum of 5mm was immersed in the oil. A large, wide reservoir approximately 90mm in diameter and 40mm deep held 237 ml of oil in order to minimize oil level fluctuation as the oil is wicked up into the reinforcement during saturation. A timer was started and images taken at specified intervals for an hour, or until complete saturation was achieved. For measurement calculations a scale was placed next to the samples and captured in each photo so during analysis a correlation between millimeters and pixels could be set.

An initial issue discovered during experiments was the difficulty to see the canola oil's progression through the fabrics in the fabric dip tests. Many different solutions were explored including food coloring, ink, soap dye, oil stain, and red chili oil, but all had poor results. Both food coloring and ink were immiscible in the oil. The soap dye, oil stain, and red chili oil were

miscible, but as the mixture progressed through the fabric the coloring slowly faded, as it appeared the coloring was being filtered out. Other similar experimental designs have employed fluorescent dyes to monitor saturation in fiberglass (Lebel 2014). Adding a few drops of Universal AC UV Dye to the canola oil and implementing a black light, the progression could easily be seen in both the fiberglass and carbon fiber samples. To the author's knowledge, this is the first known published use of fluorescent dyes with carbon reinforcements as carbon is opaque, but the polymer stitching threads in this NCF allowed tracking of the flow-front.

Non-compressed dip tests were performed with a single ply fiberglass and carbon fiber fabric. Three tests were performed in both the warp and weft direction and for each of the two reinforcement types for a total of 12 tests. Images were taken of the fiberglass tests at an interval of 5 minutes until complete saturation was achieved. The carbon fiber samples filled at a much slower rate (lower permeability and higher uncompressed fiber content) resulting in images being taken every 5 minutes for the first 30 minutes, then every 10 minutes for the last 30 minutes.

Compressed dip tests were performed with four ply's of each fabric. The samples were held between two 13mm thick sheets of acrylic that were clamped together at each of the four corners (Figure 3-2). Spacers ran the vertical length of each side of the fabric and were adjusted to a specific distance to create the desired fiber volume. Sealing putty was also applied along the lengths of the fabric between it and the spacers to minimize race-tracking and allow for a more homogeneous, one-dimensional flow direction (consistent saturation). The fiberglass tests were performed in the warp and weft direction for 40, 45, and 50 percent fiber volume, while the carbon fiber was performed in the warp and weft for 50, 55, and 60 percent fiber volume. The fiber volume was determined by the following equation:

$$v_F = \frac{nA_W}{w\rho_F} \tag{3-1}$$

where $v_F$, $n$, $A_W$, $w$, and $\rho_F$ represent the fiber volume percent, number of plies, areal weight of the fabric, thickness, and density of the fibers, respectively. Each combination of fiber orientation and fiber volume was performed three times for a total of 36 experiments.

**Figure 3-2: Experimental Setup for Compressed Fabric Dip Tests**

### 3.3.2 DIC/DAQ Vacuum-Bag Infusions

Vacuum-bag infusions were performed in order to observe flow behavior using a combination of digital image correlation (DIC) and data acquisition (DAQ) systems. Infusions were performed on both carbon fiber and fiberglass samples, cut to dimensions of 400 mm by 250 mm, stacked four ply's thick, all ply's being longest in the warp direction. A special plate

was manufactured from 6061 aluminum to allow for the connection of six Dwyer pressure transducers (Model 628-00-GH-P9-E1-S1) (Figure 3-3).

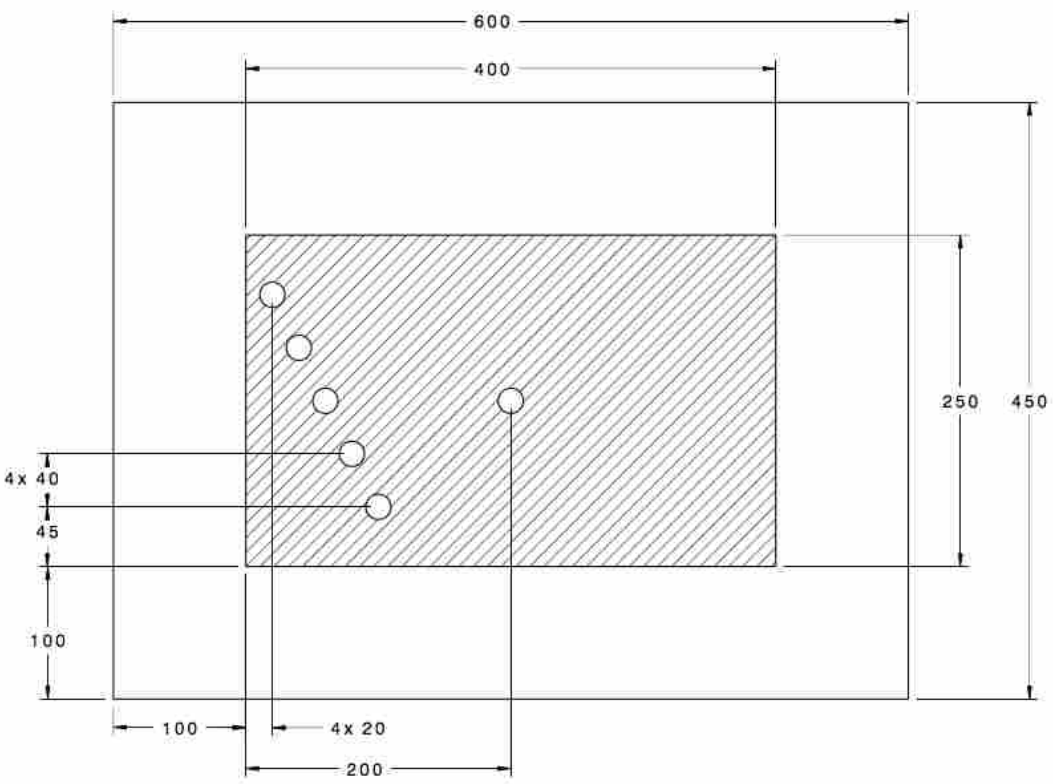


**Figure 3-3: DIC/DAQ Test Plate Drawing**

Fabric was placed in the designated area on the aluminum fixture plate. Strips of distribution media were then placed at both the inlet and vent ends of the fabric. Spiral tubing was placed on top of the distribution media and connected to the inlet and vent tubing. A vacuum bag was then placed over the layup and held to the plate using sealant tape. Fabric was butted up against the sealant tape to minimize race-tracking during infusion. With the inlet tubing sealed off, the layup was put under vacuum until the fabric was compressed. A 1-inch wide strip of masking tape was ran lengthwise down the middle of the layup and a film of white paint was applied to the vacuum bagging. Once the white paint was dry, dots/speckles of black paint were

applied over the white paint for contrast. The masking tape could then be removed so that resin flow could be observed during the infusion in a thin strip along the flow direction (Figure 3-4).

**Figure 3-4: Experimental Setup of DIC/DAQ System**

With layup complete, it could then be placed under the DIC cameras and the transducers were connected to the DAQ system. The inlet tubing was placed in an oil pot that was left open to ambient pressure. The vent tubing was connected to a closed catch pot and brought to vacuum pressure (0-10 mbar absolute pressure). A shim was placed on top of the layup to prevent caliper indentation into the vacuum bag, and calipers were used to measure the thickness or height of the fabric to use as a basis for calculating thicknesses from the DIC's displacement data. After both DIC and DAQ systems began collecting data, vacuum was removed and the fabric was allowed to relax, so as to verify and calibrate the pressure readings from the measured DAQ electrical signals. Vacuum was then reapplied to the layup, the inlet tube opened to the oil pot commencing infusion, and the test was allowed to run until complete saturation of the fibers was achieved.

# 4 RESEARCH RESULTS AND ANALYSIS

## 4.1 Fabric Dip Tests

### 4.1.1 Height vs. Time Data Acquisition

With all fabric dip tests, both uncompressed and compressed, fluorescent dyed canola oil was allowed to saturate up the fibers (Figure 4-1) until the flow front reached the top of the sample. At various time intervals the height was measured to give a relation of height versus time for oil saturation.

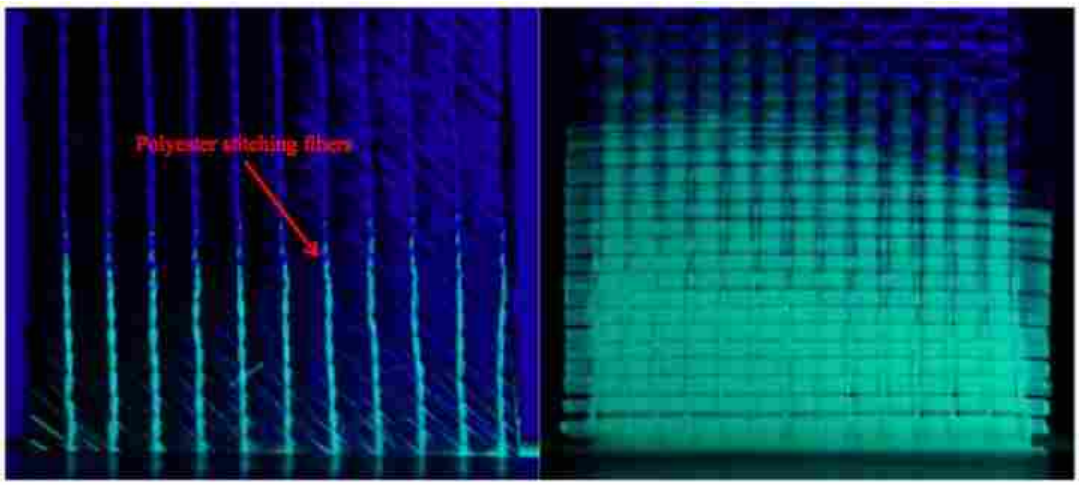


**Figure 4-1: Partially Saturated Carbon Fiber (Left) and Fiberglass (Right) Fabrics**

A similar test was presented in the literature (Amico 2000). This technique was performed in a similar study (Lebel 2014) using fluorescent dye to visually track and measure

capillary flow in the same, or at least similar JB Martin fiberglass fabric. It has generally been assumed that the same experiment could not be performed with carbon fabrics because of their opaque characteristic, i.e not capable of transmitting light such as translucent fiberglass. But as seen in Figure 4-1, the stitching fibers (common to high performance dry fabrics such as non-crimp fabrics and uni-directional weaves) are a semi-translucent polymer (polyester), allowing enough light transmission to indicate rise of the flow front.

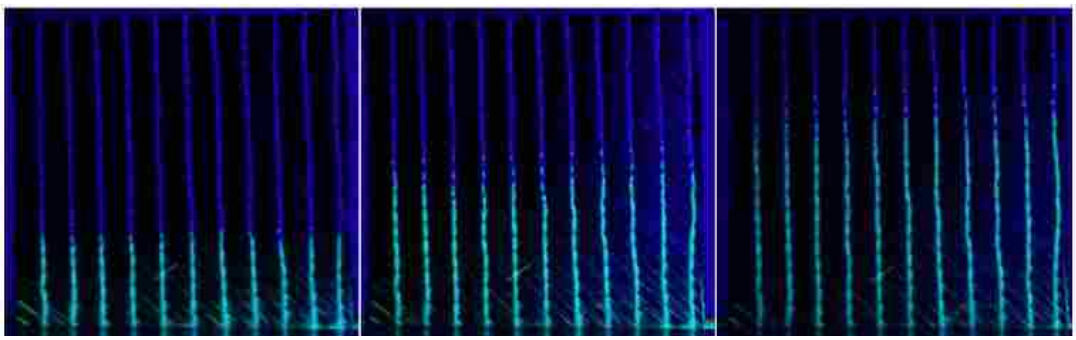

**Figure 4-2: Flow Front Advancement in Carbon Fiber at 5, 20, and 50 Minutes**

Photographs were analyzed using freeware software (Image J 2015). An initial photo had been taken with a scale next to the fabric so a relationship of pixels to mm could be developed to measure the height of saturation in each subsequent photograph. The image channels were then split from full color images to red/green/blue-based, and only the green frame was selected. An algorithm for the threshold was then ran to create a binary image based on a threshold gray value for ease in measuring the flow front height (Figure 4-3). The lengths of the leading and trailing flow fronts were recorded, the trailing flow front being where dye was seen in the inter-tow gaps (45° angle to flow) indicating inter-tow saturation. But this flow front was harder to detect than the leading flow front (height of the flow in the stitching), thus the leading flow front was used in

further calculations. Although all example photos seen so far depict uncompressed tests, the acquisition of height vs. time data in the compressed tests followed the same methodology.

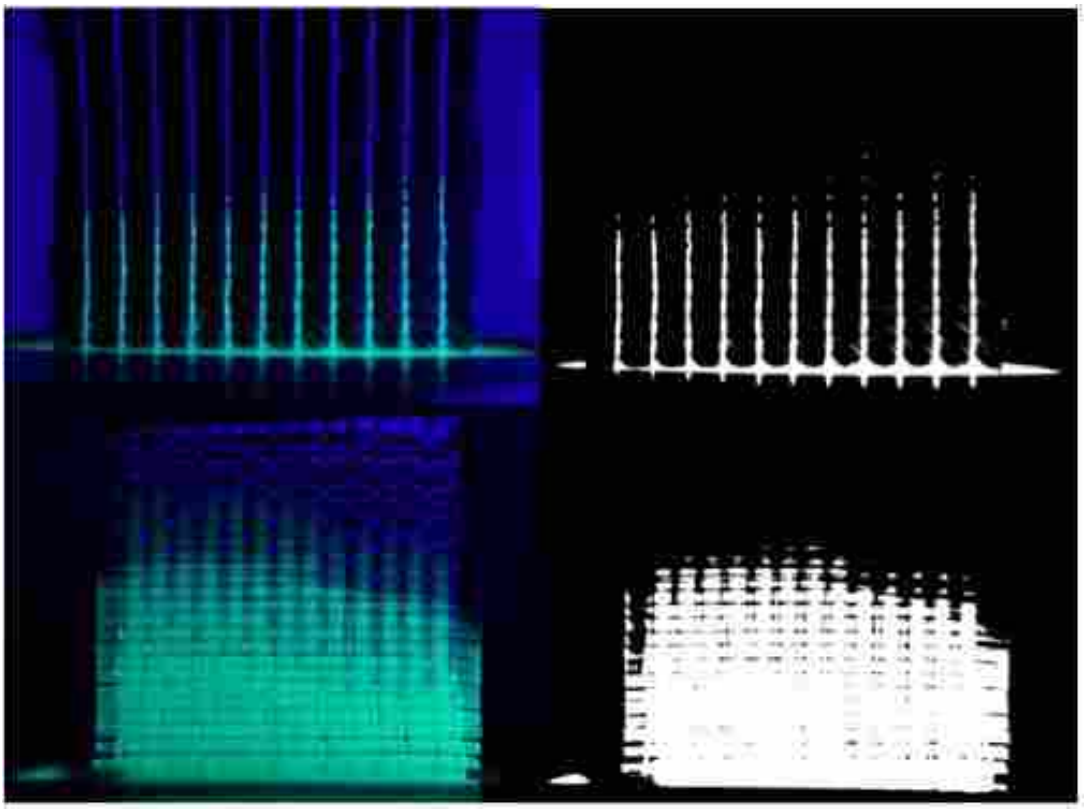

**Figure 4-3: Original and Binary Image of Saturated Samples**

### 4.1.2 Capillary Pressure Calculation Methods

Three methods were used to infer the capillary pressure from the height vs. time data measured in the dip tests.

#### 4.1.2.1 Method A – Neglecting Gravity

Resin flow during composites processing has traditionally been modeled with Darcy's Law for porous media theory (Darcy, 1856). For one-dimensional flow neglecting the effects of

gravity, the velocity of flow can be integrated with respect to time to give the length versus time relationship:

$$\frac{h^2}{t} = \frac{2K\Delta P}{\varphi\mu} \tag{4-1}$$

Where $h$ is length of flow going up through the height of the sample, $t$ is time, $K$ is permeability, $\Delta P$ is the change in pressure gradient, $\varphi$ is porosity, and $\mu$ is the viscosity of the fluid. In a dip test, the only pressure driving flow is the capillary pressure, thus $P_{cap}$ can be substituted for $\Delta P$ and then $P_{cap}$ can be calculated from any data point of ($h$,$t$):

$$P_{cap} = \frac{h^2\varphi\mu}{2Kt} \tag{4-2}$$

Assuming known values for the porosity, viscosity and permeability. The permeability, *K,* was experimentally determined, but the details will be presented later in this thesis along with the tests used to determine it. The porosity was estimated as the non-compressed wet porosity, which was also determined in experiments described later in this paper. The viscosity of the canola oil test fluid was determined experimentally with a Brookfield viscometer at various temperatures to build a model to predict the viscosity at any particular ambient temperature.

Equation 4-2 results in effective $P_{cap}$ values at each of the data sampling time intervals. Flow front progression is never very regular due to micro-variation in the textile (Vernet, 2014). An averaged value for $P_{cap}$ can be determined by fitting a linear equation to a plot of $h^2$ vs. $t$, where the slope, $M$ equals:

$$M = \frac{2KP_{cap}}{\varphi\mu} \tag{4-3}$$

The slope is averaged across all data points, and thus the average $P_{cap}$ across the experiment can be determined by solving Equation 4-3 for $P_{cap}$. These forms of Darcy's Law are commonly used in experimental permeability determination (Vernet 2014).

#### 4.1.2.2 Method B – Partially Accounting for Gravity

The second method for determination of $P_{cap}$ only partially accounts for the effects of gravity. The slope of $h^2$ vs. $t$ was again determined for each sample, assuming a linear profile exists, which again neglects gravity. A function for the non-squared $h(t)$ can be determined by taking the square root of that linear fit, including the slope, $M$ of that linear profile:

$$h = \sqrt{Mt} \tag{4-4}$$

Taking the derivative with respect to $t$ gives us the inferred slope at any point:

$$\frac{dh}{dt} = \frac{M}{2}(Mt)^{-1/2} \tag{4-5}$$

Equation 4-1 can be modified to incorporate the effects of gravity. Beginning with the non-integrated velocity form of Darcy's Law, and incorporating gravity as well as capillary pressure as the only driver for flow (Amico 2000):

$$\frac{dh}{dt} = \frac{K}{\mu\varphi}\frac{P_{cap}-\rho g h}{h} = \frac{KP_{cap}}{\mu\varphi h} - \frac{K\rho g}{\mu\varphi} \tag{4-6}$$

where $K$, $\mu$, $\varphi$, $P_{cap}$, $\rho$, and $g$, are the permeability, viscosity, porosity, capillary pressure, liquid density, and gravitational constant, respectively. The right-most term represents the contribution of gravity, decreasing the flow rate $dh/dt$ of the infusion. At short flow distances, the effects of gravity are small, and the right-most term in Equation 4-2 can be disregarded, reverting back to Equation 4-1. But in this calculation method, although the slope was determined assuming a

linear profile in $h^2$ vs. $t$, that slope is used in Equation 6, leaving the gravity term in place. Substituting Equation 4-5 ($dh/dt$) into Equation 4-6 and solving for $P_{cap}$:

$$P_{cap} = \pm h\left(\frac{M\mu\varphi}{2K\sqrt{Mt}} + \rho g\right) \tag{4-7}$$

This function, given the height and time for a given data point, is Method B for determination of $P_{cap}$.

#### 4.1.2.3 Method C – Fully Accounting for Gravity

A solution was presented in Amico (2000) to determine $P_{cap}$ from a dip test while fully accounting for gravity. Equation 4-6 (Darcy's Law with the gravity term) can be converted to a linear equation:

$$\frac{dh}{dt} = M\frac{1}{h} + B \tag{4-8}$$

where:

$$M = \frac{KP_{cap}}{\mu\varphi}, B = \frac{-K\rho g}{\mu\varphi} \tag{4-9}$$

This can lead to confusion, as $M$ in this case is the slope ($dh/dt$ vs $1/h$) of a graph of data including a different slope ($h$ vs. $t$). The slope $dh/dt$ in this case is not assumed linear but approximated at each data point by taking the difference in height and time in succeeding sampling steps. To minimize bias towards the initial fast flow, the instantaneous slope was approximated by averaging the difference in heights and time for three successive measurement points:

$$\frac{dh}{dt} = \left(\frac{h_2 - h_1}{t_2 - t_1} + \frac{h_1 - h_0}{t_1 - t_0}\right)\frac{1}{2} \tag{4-10}$$

Each value of this slope is plotted against the corresponding value of $1/h$, and the slope $M$ and intercept $B$ can be fitted from the resulting graph as per Equation 4-8.

As the permeability is difficult to measure with certainty, the two parts of Equation 4-9 (for slope and intercept) were combined by solving each for $K$. The resulting combined equation was then solved for $P_{cap}$:

$$P_{cap} = \frac{-M\rho g}{B} \tag{4-11}$$

This gives an average value for $P_{cap}$ over the entire test range based on the fitted $M$ and $B$ of the graph of $1/h$ vs. $dh/dt$.

### 4.1.3 Uncompressed Dip Test $P_{cap}$ Results

Figure 4-4 shows the measured values of $h^2$ versus time. Error bars denote the standard deviation over the 3 samples averaged for each data point. As seen, the flow is fairly Darcian, i.e. the slope, $M$, is fairly constant which also implies that the permeability, pressure gradient, porosity and viscosity remain fairly constant throughout the test. In this case, of course, the pressure gradient is not typical to composites processing, where over-pressure or vacuum pumps are applied to drive the flow. Instead, these dip tests only employ capillary pressure to drive the flow, and the flow is impeded by gravity, which reduces the pressure gradient as the flow front rises through the sample. Some sagging flow fronts can be seen towards the right side of the graph – implying that gravity is slowing things down, although to a seemingly small degree for all but the glass weft experiments, which seem to hit a maximum height and stay there. The linear fit for glass-weft was thus only fit to the data up to 1,200 seconds.

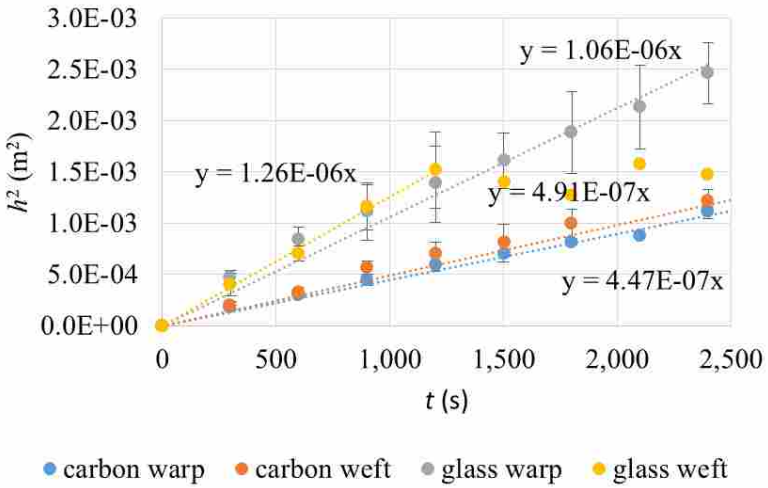


**Figure 4-4: $h^2$ vs. $t$ Average Profiles for Uncompressed Dip Tests**

After calculating the $P_{cap}$ for each time interval, the average $P_{cap}$ value for each material and orientation was plotted against $h$ to observe the amount at which $P_{cap}$ is changing as the flow advances. This is shown in Figure 4-5 for Method A, Figure 4-6 for method B, and Figure 4-7 for method C.

Figure 4-5 shows linearly decreasing $P_{cap}$ with flow height for all but one sample. This decreasing trend is assumed to be due to the effects of gravity in that the flow rate is being slowed down more and more by gravity as the test goes on, but the model to determine $P_{cap}$ has no way to account for that except to blame the decreasing flow rate on a decrease in the driving pressure. The slope ranges from approximately 3 to 8 kPa/m for all of the four averaged plots. The hydrostatic pressure head due to gravity is the product of the density, gravity and height, the pressure divided by the height (slope) in Figure 4-5 should be approximately the product of density and gravity, which in this case is about 9 kPa/m. This value is close to the range in slopes, lending credibility to gravitational effects. Note that little difference exists between orientations (warp vs. weft). Also, the carbon data shows about twice the capillary pressure as

glass, an understandable result due to the higher fiber packing in carbon compared to the glass fabric.

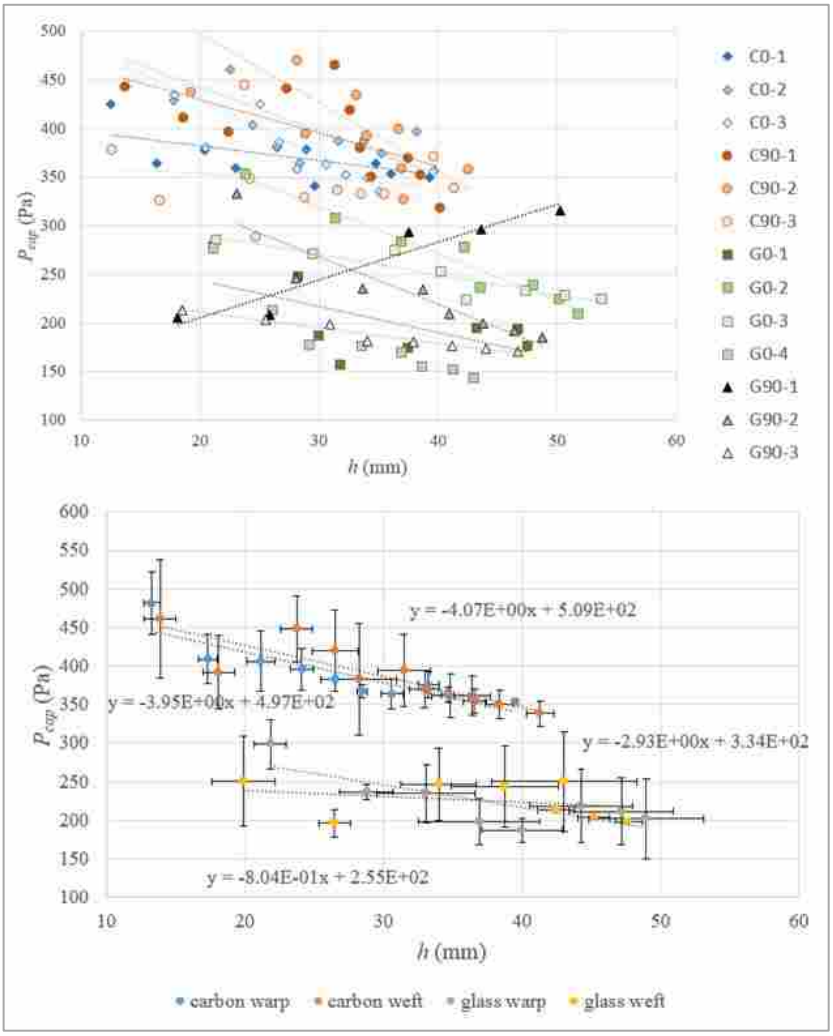


**Figure 4-5: Uncompressed $P_{cap}$ Results for Method A: Each Sample (top); Averaged by Orientation (bottom)**

Figure 4-6 (Method B) shows increasing slopes instead of decreasing slopes as were seen in Figure 4-5 (Method A). This is probably due to the incongruence of not accounting for gravity to determine *dh*/*dt*, and then using that value in an equation with a gravity term. The slopes in this case are around 7-8 kPa/m for all but the glass weft averaged profiles, an even closer match

to the product of gravity and density as determined above. Note that in both cases, there is again little difference between flow orientations, with error bars overlapping each other for the 0 and 90 degree tests. The agreement is especially clear for carbon in the averaged data, but even glass has good agreement when looking at the individual tests. Carbon again results in higher $P_{cap}$ than glass.

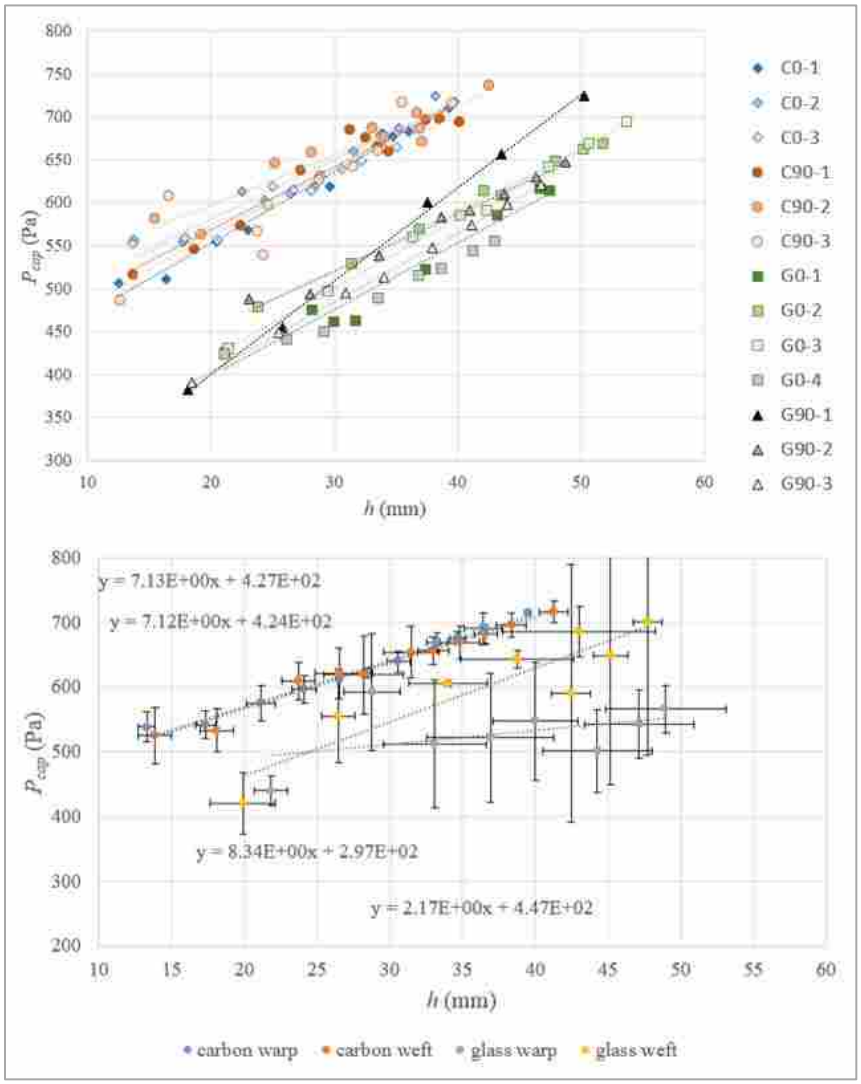


**Figure 4-6: Uncompressed $P_{cap}$ Results for Method B: Each Sample (top); Averaged by Orientation (bottom)**

Figure 4-7 (Method C) only shows results for the fitting of *M* and *B* to the data, for the purposes of determination of the average capillary pressure by Equation 4-11. The fitted values for *M* and *B* are seen on the charts. The initial data point (at the fastest flowrate) was neglected in these fits as it was far from the rest of the data (up and too the right on this figure) and off the linear fits from the other data points. The resulting profiles show fair linearity, justifying this calculation method.

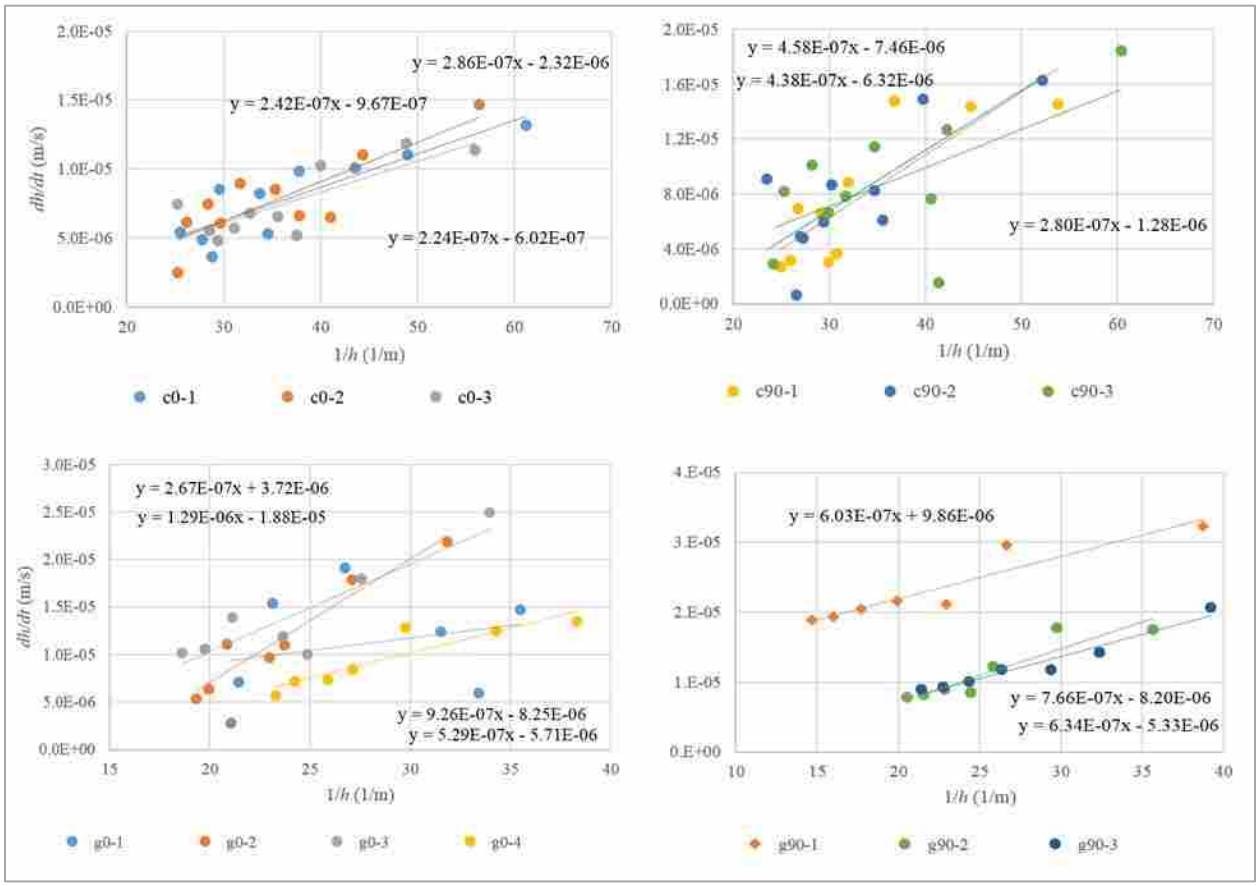


**Figure 4-7: Uncompressed Method C Plots for Determination of Average $P_{cap}$: Carbon (top), Fiberglass (bottom)**

The average $P_{cap}$ value through each material and flow orientation was computed for each test method, by using the average slope method described above for both Methods A and

C, and by simply averaging the $P_{cap}$ values seen in Figure 4-6 for Method B. These single $P_{cap}$ values (Figure 4-8) naturally do not say anything about the increasing or decreasing trends in $P_{cap}$, although it is assumed that $P_{cap}$ should remain fairly constant when accounting for other non-capillary phenomenon, and such average numbers allow a clear comparison between samples and test methods. Figure 4-8 also includes the capillary values determined by Method A when using both the upper/leading flow front height (top) and lower/trailing flow front height (bottom). Figure 4-3 demonstrates this, where the upper flow front is represents the capillary flow in between the fiber bundles or through the stitching. The lower flow front represents the point at which the entire cross-section is saturated with resin, and is more difficult to measure. As seen in Figure 4-8, using the lower flow front results in lower determined $P_{cap}$ values as the flow rate is slower, and more scatter due to the greater difficulties in measuring this with precision. As the upper flow front is associated with the first capillary flow, this is assumed as the more accurate method for the effects on flow, as well as being more precise.

Also seen in Figure 4-8 are the low $P_{cap}$ values when gravity is neglected, and the higher values when it is accounted for. Method C, giving credit to the effects of gravity, understandably results in the highest $P_{cap}$ values. This method is thought to be most accurate due to the gravity term, but results in less precision than the other methods, probably due to the increased degree of slope approximations involved. The carbon warp values for method C are particularly high, but with a high degree of variation as well. For all methods, carbon achieves a slightly higher $P_{cap}$ than glass.

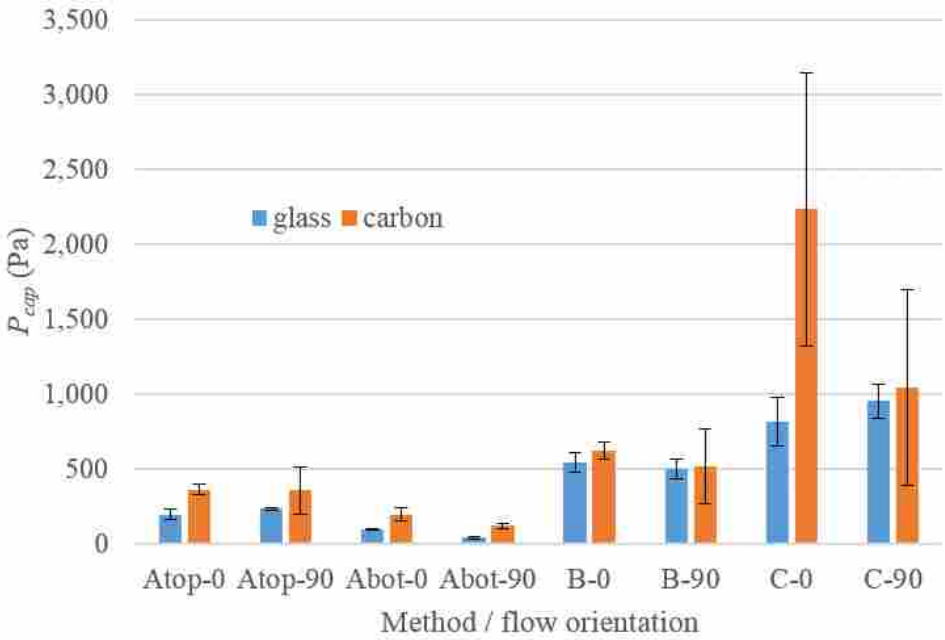


**Figure 4-8: Average $P_{cap}$ Values for Uncompressed Flow Tests**

### 4.1.4 Compressed Dip Test $P_{cap}$ Results

Figure 4-9 shows the $h^2$ vs. $t$ profiles for all material, orientation, and thickness combinations. In contrast to Figure 4-4 (uncompressed tests), these profiles who definite sagging in all cases, implying that gravity is playing a greater role at slowing the flow down as the sample gets higher. The role of gravity is assumed to be playing a higher role here than in the uncompressed test due to the slower flow / greater reduction in pressure caused by the greater compaction. Thus the linear fits for $P_{cap}$ determination by Method A were done using only the data up through 1800 s for carbon, and 360 s for glass, to reduce the non-linearity caused by gravity (Figure 4-10). Note that although the nonlinearity is reduced, there is still some sagging in the right side of each profile even at these short times.

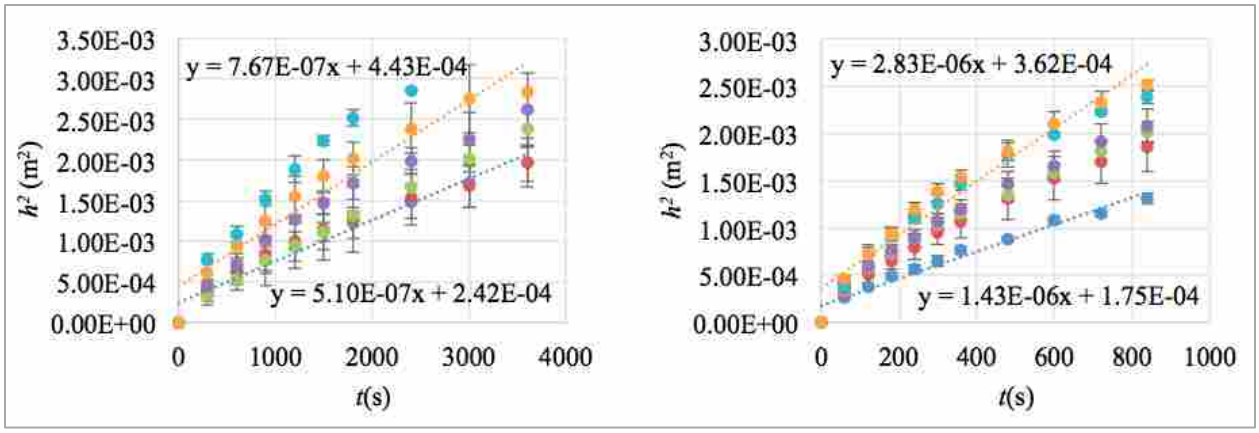


**Figure 4-9: $h^2$ vs. $t$ Average Profiles for Compressed Dip Tests: Carbon (left), Fiberglass (right)**

Figure 4-11 through 4-13 show the same graphs as Figure 4-5 through 4-7 but for the compressed dip tests, including the three different thickness (compaction) levels. The figures include first a graph of the individual plotted data points for each sample, and then a graph of those data points averaged by orientation with errors bars representing standard deviation. Method A (Figure 4-11) again shows decreasing slopes due to neglecting gravity in the flow calculations. Method B (Figure 4-12) again reverses this trend and shows positive slopes. The data in Method C (Figure 4-13) appears to be fairly linear again, thus validating this calculation method.

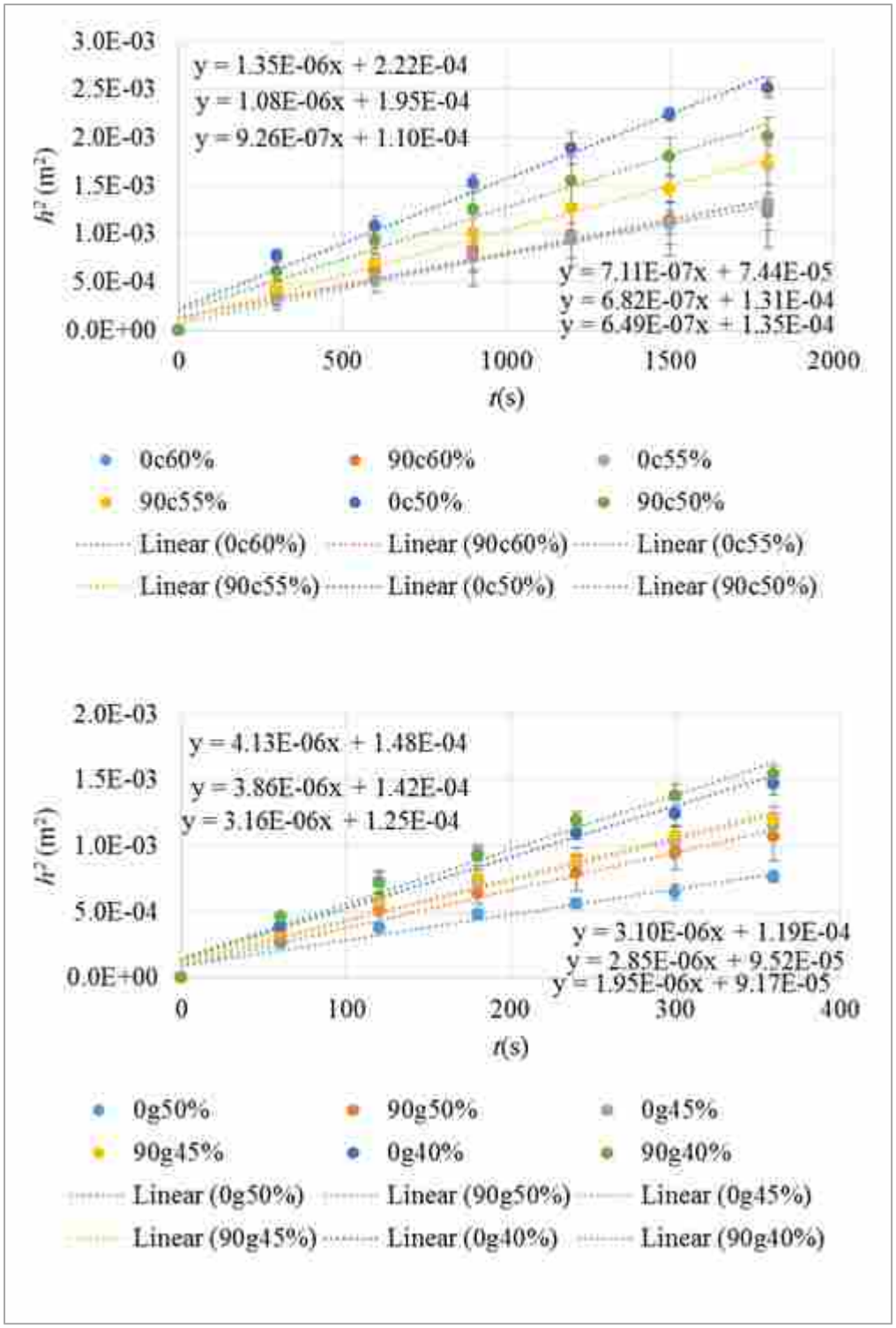


**Figure 4-10: Linear Fits for Only First Few Data Points from Figure 4-9**

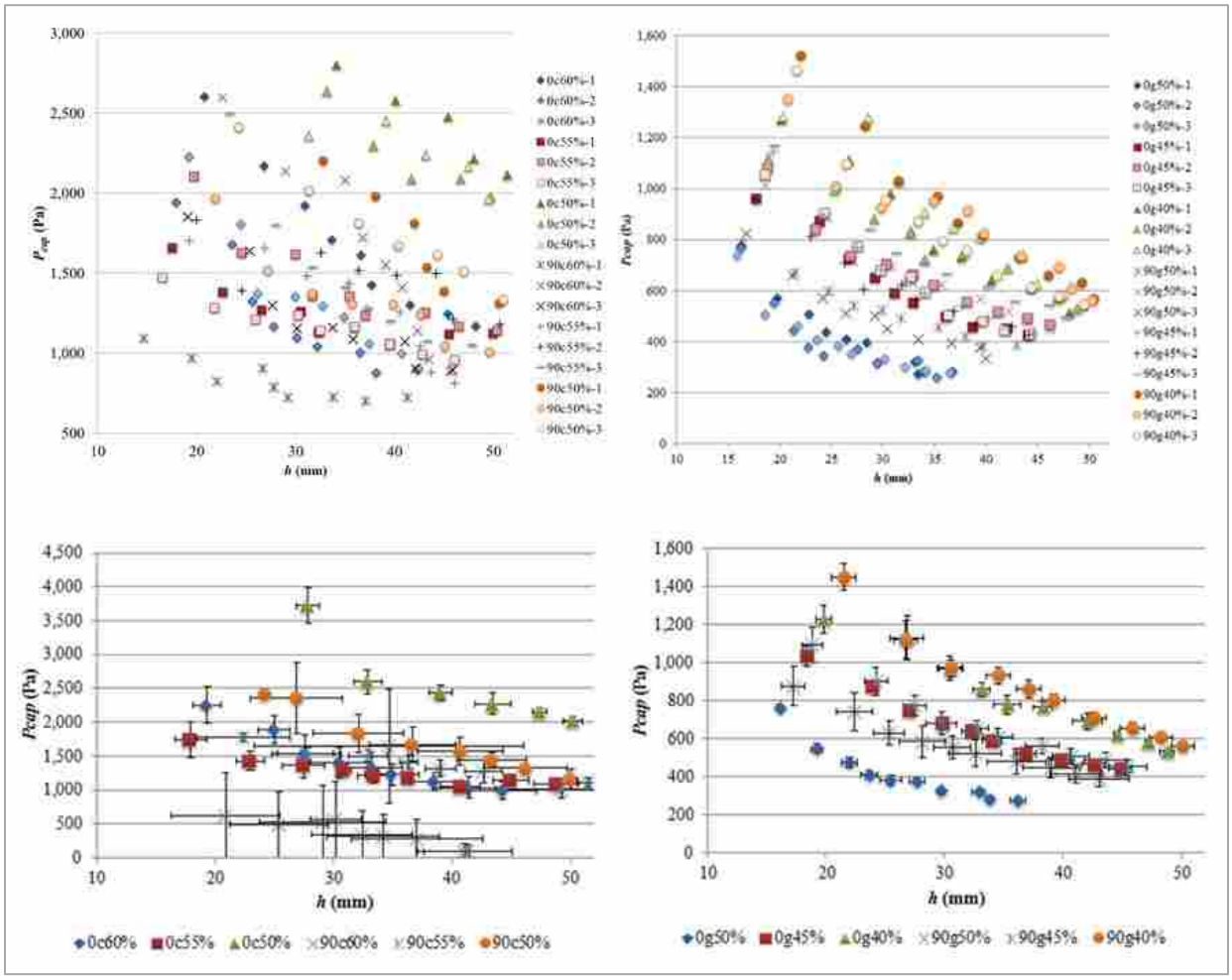


**Figure 4-11: Compressed $P_{cap}$ Results for Method A: Carbon (left), Fiberglass (right); Individual (top), Averaged (bottom)**

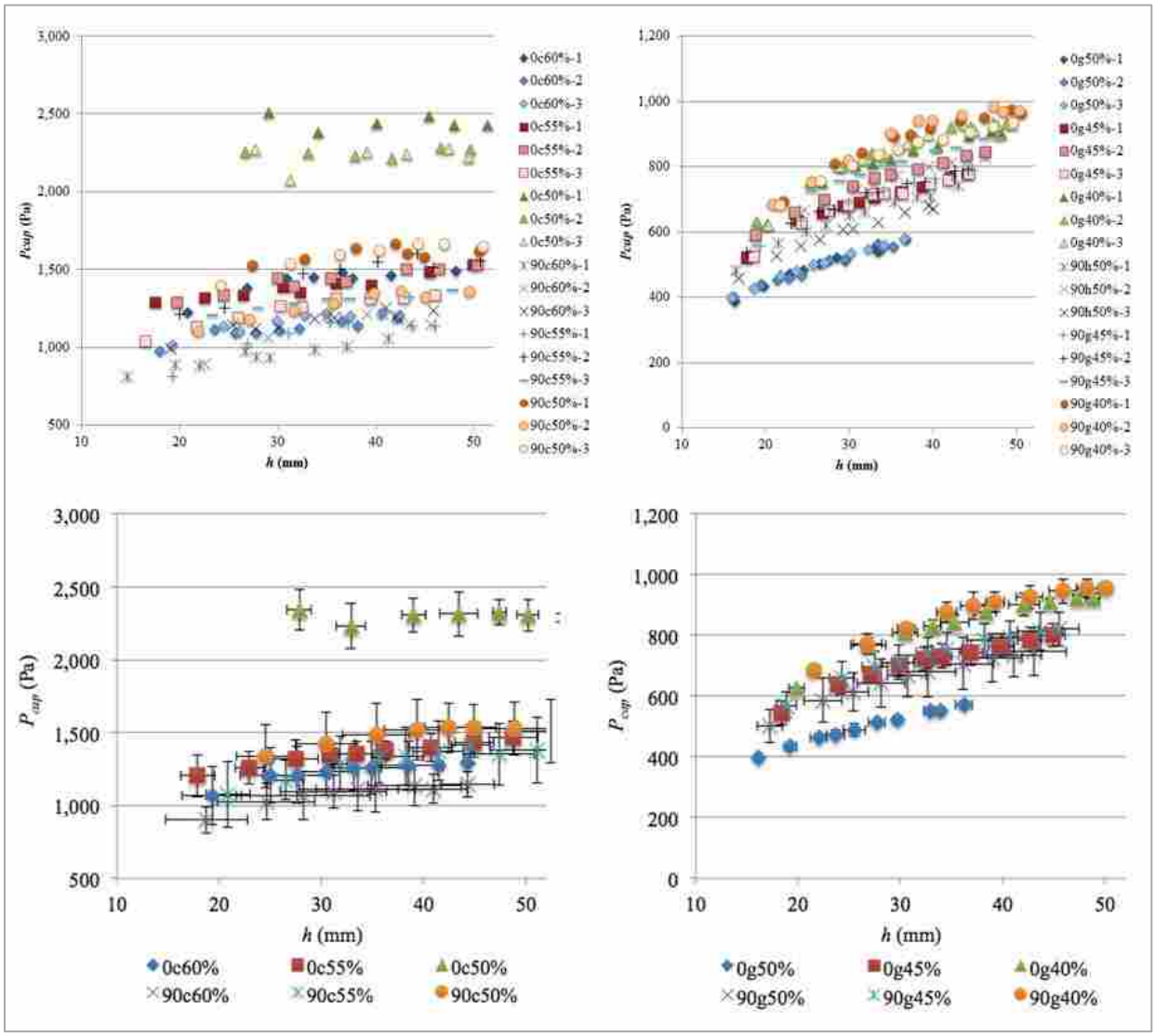


**Figure 4-12: Compressed $P_{cap}$ Results for Method B: Carbon (left), Fiberglass (right); Individual (top), Averaged (bottom).**

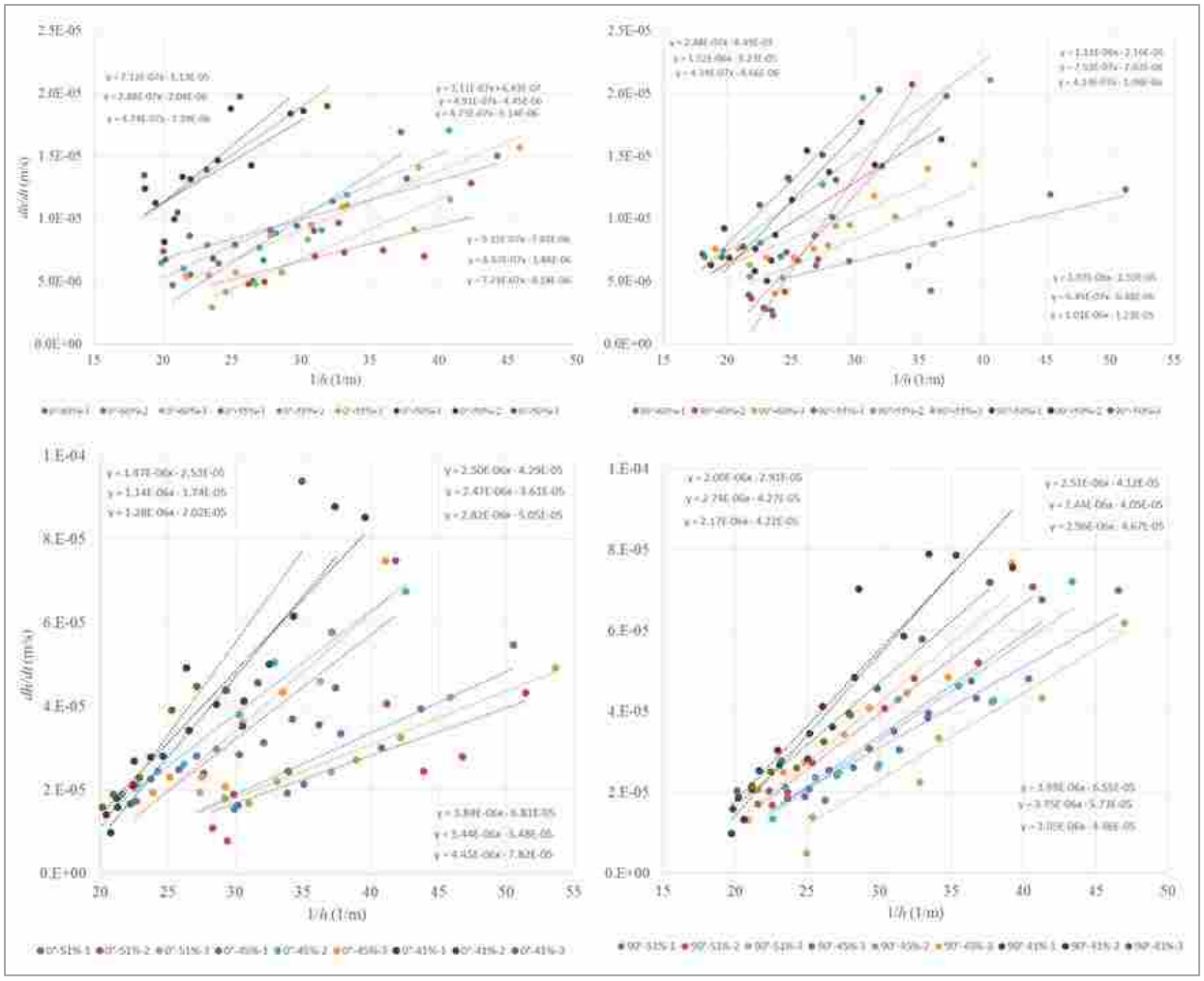


**Figure 4-13: Compressed Method C Plots for Determination of Average $P_{cap}$: Carbon (top), Fiberglass (bottom)**

Figure 4-14 shows the averaged values for each flow test again (as in Figure 4-8), this time for the compressed tests. Carbon again shows higher $P_{cap}$ than glass. In the uncompressed results, Method A resulted in lower $P_{cap}$ values than Method B, but no clear difference across all fiber contents can be seen here in the compressed tests. Method C no longer provides the highest estimates of $P_{cap}$, although a high standard deviation is again seen.

The results listed here for $P_{cap}$ have been low (usually between 1 and 2 kPa) compared to the 100 kPa provided by full vacuum at sea level in common infusion processing. During resin

infusion processing, however, that maximum pressure gradient of 100 kPa only exists when the flow first enters the preform, and the pressure gradient at the flow front, driving the flow, continues to diminish as the flow moves through the fibrous reinforcement. The maximum pressure gradient is also reduced when infusing at higher altitudes than sea level. Thus the relative effects of $P_{cap}$, even at 1 kPa may become significant in flow modeling under certain slow flow conditions in composites processing.

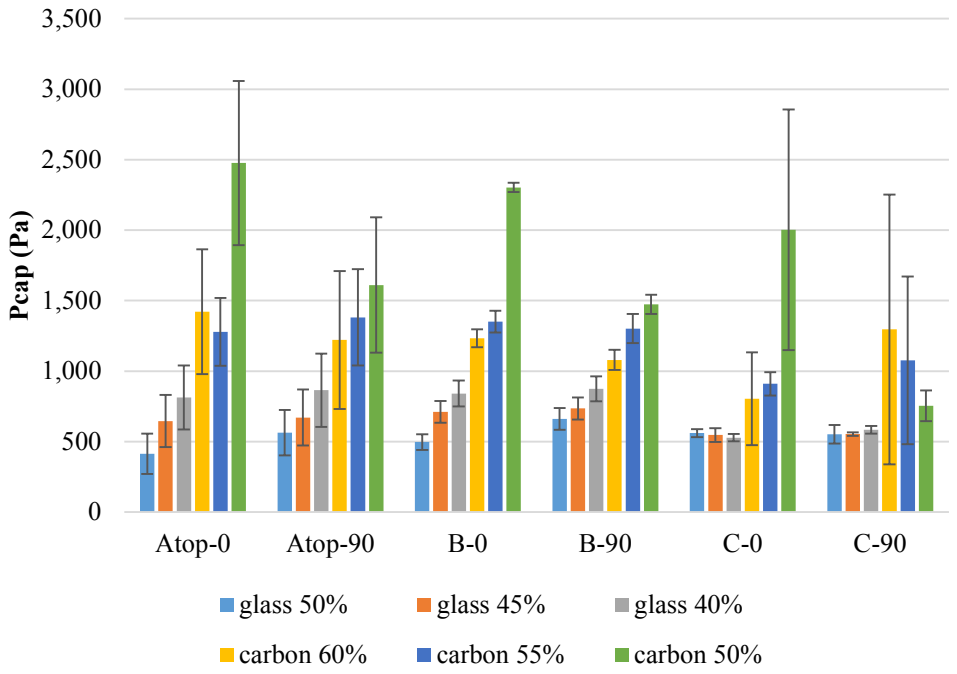


**Figure 4-14: Average $P_{cap}$ Values Throughout a Compressed Flow Test**

### 4.1.5 Comparison of $P_{cap}$ Results with Prediction

A classic equation to describe capillary flow was derived (Ahn 1991) from capillary flow modeling and adapted to flow in a fibrous reinforcement:

$$P_{cap} = \frac{F}{D_f} \cdot \frac{1-\varphi}{\varphi} \gamma cos(\theta_{CD}) \tag{4-12}$$

where $F$, $D_f$, $\varphi$, $\theta_{CD}$, are a form factor describing the flow direction in relation to the fiber orientation, diameter of a single fiber, the surface tension of the liquid, and the dynamic contact angle between the liquid and solid fiber surface, respectively. The difficulty with using this equation is the difficulty in measuring the form factor and the dynamic contact angle. The latter requires macro lens video of the capillary rise on a single 7-10 micron fiber as it is drawn out of the liquid (Lee, 1996). But general comparisons can be made by relative estimates of these variables.

In Equation 4-12, $F$ is the form factor for alignment of the fibers to flow, being 4 for along the fibers (parallel flow), and 2 for perpendicular flow. Both of these fabrics are nearly isotropic in permeability (as discussed later in this paper). The carbon fabric is a balanced +45/-45 biaxial fabric, with a very small stitching fiber being the only difference in flow orientation. The fiberglass fabric is an unbalanced biaxial weave, but both warp and weft only differ a small amount in areal weight. This is evident in the $P_{cap}$ results, as there seems to be no difference in flow orientation, implying that the form factor is fairly uniform for both warp and weft in both materials. The porosity, surface tension, and fiber diameter are constant throughout a flow test. The dynamic contact angle has been shown to slightly decrease as the velocity decreases (Lee, 1996), but the magnitude of this change on $P_{cap}$ in Equation 4-12 is difficult to ascertain without performing difficult measurements of $\theta_{CD}$. Other possible sources of variation in the variables are:

1. In the uncompressed dip tests, the fluid flow is not completely 1D in the upward direction, but flows off and down off the sides also.
2. Porosity may be changing with increasing lubrication, making a gradient in porosity along the fabric from the fluid pool to the flow front.

If we neglect these two possible sources of variation, then $P_{cap}$ should remain constant throughout an experiment. Of course, methods A and B have shown to have regular gradients one way or the other, which is assumed to be due to gravitational effects not being accounted for.

Compressed fabrics showed a higher $P_{cap}$ than non-compressed. This is probably due to the higher fiber volumes that were tested with the carbon fiber, which resulted in a higher compression than the fiberglass tests, and would predict by Equation 4-12 a rise in $P_{cap}$ along with the decrease in porosity from higher compression.

For method A calculation, the $P_{cap}$ values for carbon are a little less than twice that of the fiberglass $P_{cap}$ values (Figure 4-8). As these are both biaxial NCF's, the form factor should be similar. And the differences in flow rates are thought to cause minor differences in the dynamic contact angle on similar sizing materials for both fiber types. The surface tension is equal in both cases as it's the same test fluid. Therefore the differences in fiber diameter (7 microns for carbon and 10 for glass) and porosity (63% for carbon and 67% for glass) should account for the only differences in $P_{cap}$ according to Equation 12. With the variables for each fabric type, the predicted $P_{cap}$ from Equation 12 for carbon is 1.67 times that of glass, which agrees well with the ratio seen in Figure 4-8 for method A. The lower porosity in carbon compared to glass is also assumed to cause the rise in $P_{cap}$ values seen in Figure 4-14.

In Figure 4.14, it can be noted that increasing porosity resulted in increasing $P_{cap}$ for methods A and B, while no significant trend can be seen in method C (all within each other's' standard deviation). This would seem to be a contradiction of Equation 12, as porosity is in the denominator of the equation, and increasing porosity would increase the flow rate, and correspondingly the contact angle, thus decreasing the cosine of the contact angle. These two cases would both predict decreases in $P_{cap}$, not the increases seen in Figure 4.14. One possible

explanation would again be gravitational effects; gravity becomes more relatively important as the flow slows down in more compressed samples. This may explain the lack of any clear trend in $P_{cap}$ for carbon using Method C, where gravity is accounted for, and no particular increase or decrease is seen with increasing thickness.

## 4.2 DIC/DAQ Infusion Results

Along with the dip tests, two additional types of experiments were performed; one being compressibility tests performed in another work (Hannibal, 2015), and the other were infusions monitored by a DIC/DAQ system.

### 4.2.1 Permeability Determination

The fabric permeability, $K$ that was used in later flow calculations was determined as follows.

#### 4.2.1.1 Fiberglass Permeability

The compressibility was taken from the DIC/DAQ infusion experiments that were performed as part of this study. The compressibility is the function $P_C(v_F)$ representing the compaction pressure needed to achieve a given fiber content. This is analogous to a stress-strain diagram in a compression test of any other material. The compressibility was determined as the measured local fabric compression pressure (ambient pressure minus the local resin pressure as measured by DAQ pressure transducers) for the measured sample fiber content (derived from the sample thickness as measured with DIC). The compressibility data derived at the 20mm, 40mm, and 60mm sensor points in fiberglass infusion number 2 and 3 (the others were regarded as

outliers) was averaged and then this data was fit to the Loos-Grimsley compressibility model (Figure 4-17), which has previously shown good fitting for high $v_F$ fabrics (George 2011):

$$1 - \left(\frac{v_{F0D}}{v_F}\right) = A_w + B_w \left(\frac{P_C}{C_w + P_C}\right) \quad (4\text{-}13)$$

Where $A_w$, $B_w$, and $C_w$ are fitting constants. $A_w$ represents a relationship between the dry uncompressed fiber content ($v_{f0D}$) and the wet uncompressed fiber content ($v_{f0W}$), $A_w$ = 1-($v_{foD}/v_{f0W}$). The average compressibility was fit with the following constants: $A_w$ = 0.0934, $B_w$ = 0.364, and $C_w$ = 44.43 mbar.

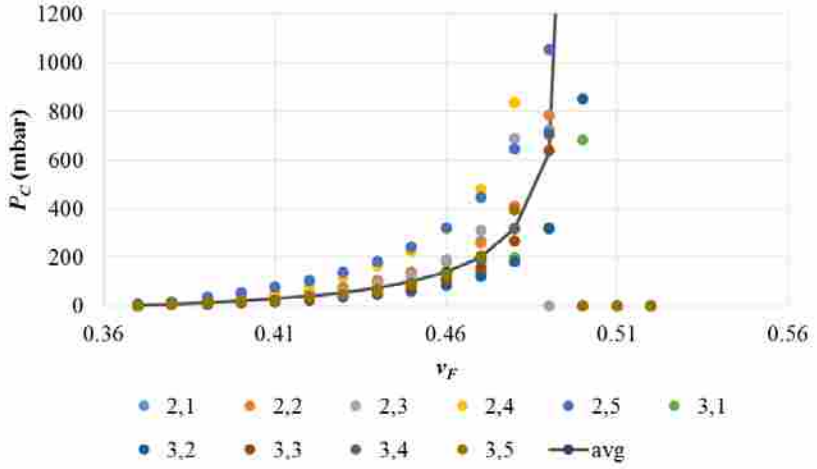


**Figure 4-15: Fabric Compressibility Measurement Results from DIC/DAQ Testing for Fiberglass Infusion 2 and 3**

This compressibility function was taken and put into a Matlab program that fits a permeability function, $K(v_F)$ (the permeability at a given fiber content; a power law function $K = A_K \cdot v_F^{BK}$) to the $L$ versus $t$ data as measured by monitoring flow front position through the DIC/DAQ infusions. The Matlab model was developed as a version of Darcy's law that accounts for the change in thickness during vacuum infusion (under a vacuum bag) as described in (Modi 2009, Correia 2004). This model was modified from the usual calculation of filling time, to fit

the permeability to the filling rate. The permeability was fit in this way to the $L$ vs. $t$ data for all 5 DIC/DAQ fiberglass infusions (all in the warp direction), and resulted in five fits for $A_K$ and $B_K$. These were averaged (Figure 4-18) to result in the follow permeability fit constants: $A_K$ = $3.9 \cdot 10^{-11}$ m$^2$ and $B_K$ = -0.56.

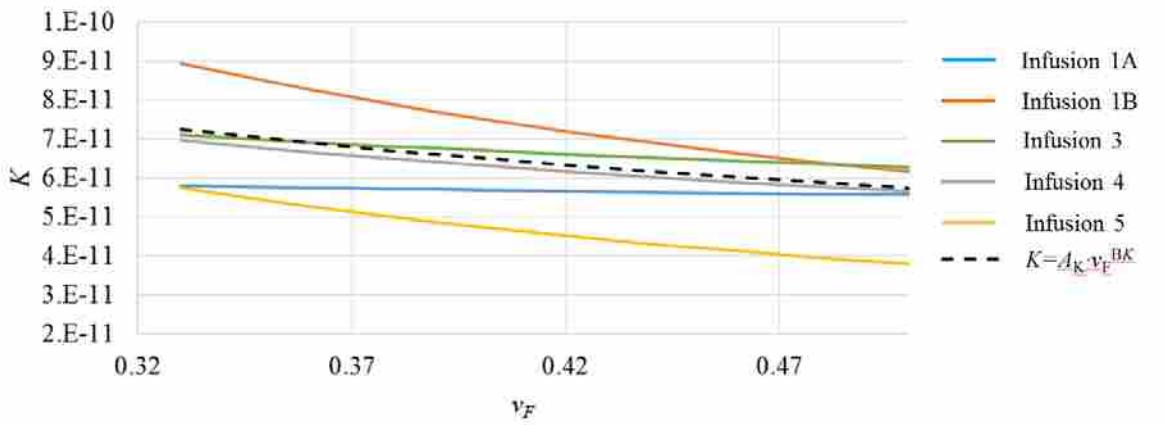


**Figure 4-16: Permeability as a Function of Fiber Content, Fit to Infusion Data, for Fiberglass DIC/DAQ Infusions**

With no infusions performed in the weft direction, and the literature showing little anisotropy in flow for this material (George 2014), the fabric was assumed to be isotropic, and these warp values were used for the weft permeability as well. A literature value at a low fiber volume (38.5%) was very high ($7.8 \cdot 10^{-10}$ m$^2$) compared to extrapolation of this fitted model which prompts the need for further testing to verify the assumption of anisotropic flow.

#### 4.2.1.2 Carbon Permeability

For carbon, the compressibility model used (Figure 4-19) was a fit of Equation 4-13 to averaged data from compressibility tests on 5 carbon fiber samples in canola oil performed elsewhere (Hannibal 2015). The compressibility model used was: $A_w$ = 0.3190, $B_w$ = 0.1827 and $C_w$ = 853.5 mbar.

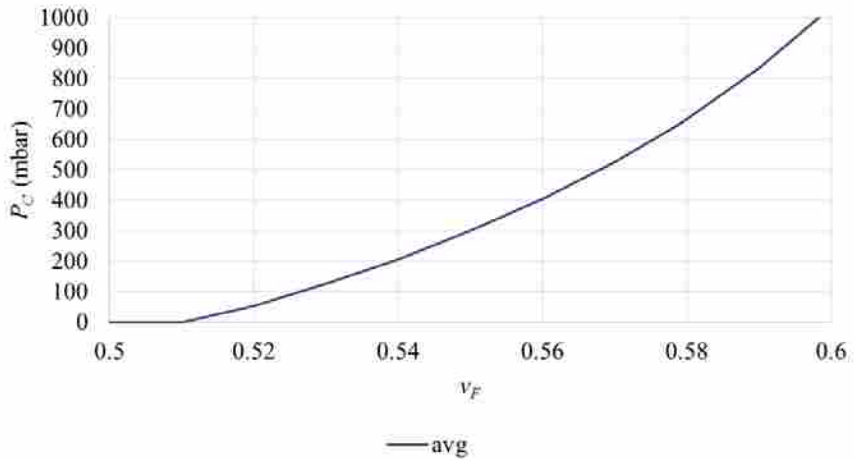


**Figure 4-17*:* Compressibility Measured from Hannibal (2015) for Carbon Reinforcement**

A total of six carbon fiber DIC/DAQ infusions were performed in this study, four in warp and 2 in weft. Values for $A_K$ and $B_K$ were fit to the $L$ and $t$ data from those experiments, and then an average permeability model made from those fits (Figure 4-20). $A_K$ and $B_K$ for warp were determined to be 1.21e-12 and -2.58, respectively. While $A_K$ and $B_K$ for weft were 1.49e-12 and -2.5, respectively.

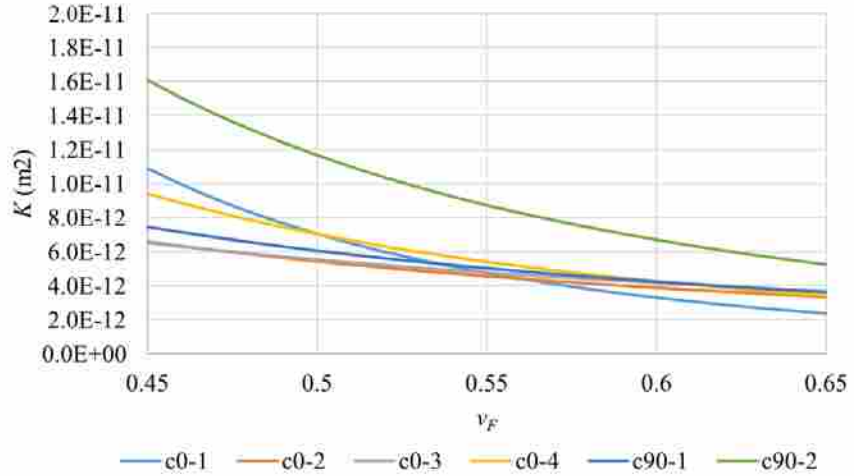


**Figure 4-18: Permeability as a Function of Fiber Content Fit to Infusion Data**

### 4.2.2 Comparison of Compressibility for Infusion and Squeeze-flow

The DIC/DAQ tests were done with vacuum infusion, which involves wetting flow, with $P_{cap}$ affecting the filling rate as it changes the pressure gradient at the flow front. The compressibility (Equation 4-13) was fit to the data at sampled time increments for the compaction pressure right at each pressure transducer and the thickness of the preform for any time at which the flow front had passed each transducer.

In contrast, the Instron-determined compressibility tests done in Hannibal (2015) = fabric soaked in bath of oil or epoxy, squeezed under Instron in compression and then soaks up the fluid again as the Instron retreats and the sample relaxes and grows in thickness. The load on the Instron minus the calculated total resin pressure on the sample resulted in the compaction at any time and sample thickness, giving the compressibility function shown in Figure 4-19. The sample has to squeeze and expand, which includes the fiber bundles, so there's capillary flow in and out of the fiber bundles, but all the fibers should already be wetted which implies that $P_{cap}$ effects are small if any. Thus although the absolute capillary pressure involved is yet unknown for both the DIC/DAQ tests in this study and the squeeze-flow tests done in Hannibal (2015), a comparison of the resultant compressibility curves should allude to the differences in capillary pressure effects. Figure 4-21 shows the average compressibility determined from all tests involving the carbon NCF for both methods. Note that the squeeze-flow compressibility in Figure 4-19 comes from the Instron load data during expansion of the wet fabric, which is thought to be most accurate to infusion. But pressure sensor data in that study suggests that the sample was not expanding as fast as the Instron cross-head, so the compression data during that test might give better data. Thus the compressibility models from both expansion and compression squeeze-flow data are shown in Figure 4-21.

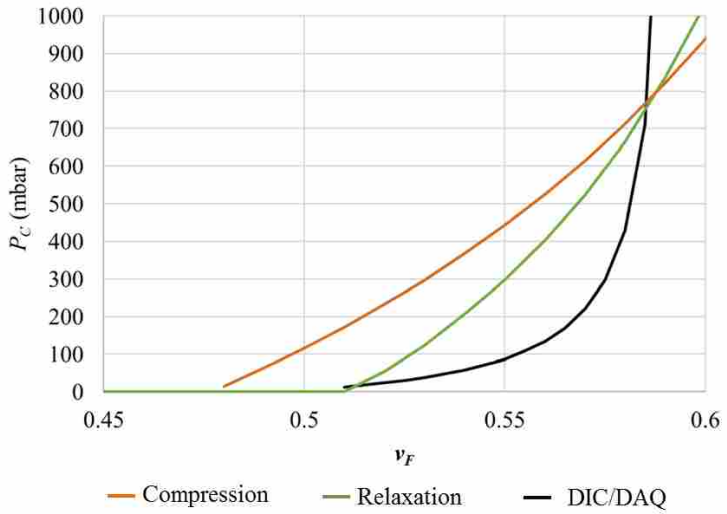


**Figure 4-19: Compressibility Determined by Instron During Squeeze Flow and by DIC/DAQ During Vacuum Infusion**

The compressibility curves in Figure 4-21 lend evidence to the suspicion that the expansion squeeze-flow data maybe be overly low compaction pressures at low $v_F$ due to the cross-head not remaining in contact with the sample. As also seen, the compliance/stiffness is very different between the two test methods. Squeeze flow testing shows a more constant stiffness, initially requiring higher compaction pressure at the same thickness, but at higher compression levels. The infusion testing shows a faster stiffening and ends up at higher compaction pressures required for any $v_F$ higher than about 0.585.

One strategy has been presented to couple both the effects of $P_{cap}$ and compressibility on flow modeling (George 2011), but no data has been yet presented that separately quantifies the $P_{cap}$ and resin pressure along the filled regime during vacuum infusion.

### 4.2.3 Pressure Gradient Comparison

In a previous study (George 2011), pressure gradients across the filled area in an infusion with carbon unidirectional weave fabric were inferred from DIC data and compressibility from

squeeze flow in Instron testing(Figure 4-20). Results from that study are shown in Figure 4-22 for a carbon unidirectional weave, where the pressure gradient is presented as a function of $\alpha$, representing the relative position between the inlet side of the reinforcement ($\alpha = 0$) and where ever the flow front is ($\alpha = 1$). Thus $\alpha = 0.5$ implies a point halfway between the inlet and the flow front, where ever that is as the flow continues to move through the sample during infusion. Note that these values for the resin pressure were not measured directly, but "inferred" (calculated indirectly) evaluating the equivalent resin pressure from the compressibility model from Instron-testing for the measured thickness from DIC.

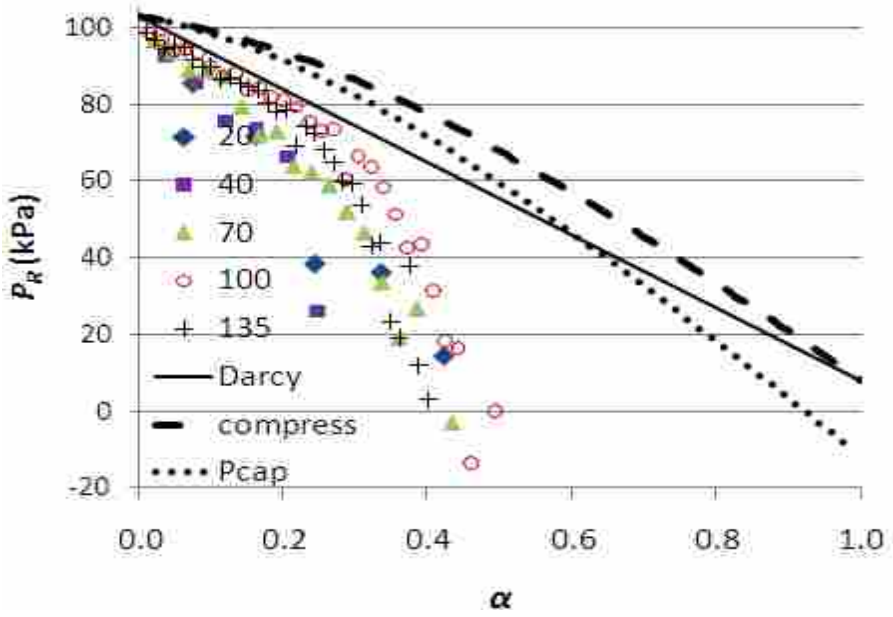


**Figure 4-20: Inferred Pressure Gradient Results (George 2011)**

In Figure 4-22, the solid black line is the pressure gradient as predicted by Darcy's Law where the fabric thickness does not change. The pressure should be a linear gradient from the inlet pressure (ambient in the case of vacuum infusion) to the vacuum pressure on the vent. The dashed line is the predicted pressure gradient from the Modi-Correia model (Modi 2008, Correia

2004) which accounts for the vacuum bag height change, and was calculated using the compressibility determined from Instron-testing. The slope of the pressure gradient at the flow front ($\alpha$ = 1) determines the filling speed at that moment during the infusion; the steeper the negative slope, the faster the infusion. Vacuum infusion allows for more thickness by the resin inlet, and thus less pressure loss there than a fixed height infusion, thus making the slope slightly steeper and faster flow.

The dotted line in Figure 4-22 was a version of the Modi-Correia model, coupled to a prediction of the contribution by capillary pressure based on the Ahn model in Equation 4-12. This is based on the pressure balance:

$$P_{ambient} - P_{vacuum} + P_{cap} = P_C + P_R \tag{4-14}$$

The colored data points in Figure 4-22 are the inferred resin pressures along the filled area when the flow front was 20 mm along in filling the sample, 40, 70, 100, and 135 mm. Those resin pressure dropped to negative "effective" pressures, much lower than the usually-assumed vacuum pressures by the flow front. This suggested that the capillary pressure contribution in Equation 4-14 may be much larger than the black dashed line model was predicting, and suggesting that the contribution of $P_{cap}$ to the overall flow rate may be much higher than previously assumed. These conclusions led to the use of DIC/DAQ in this study to try to reproduce these results, but with DAQ and pressure transducers to directly measure the resin pressure to try to validate these capillary effects.

In more recent work (Hannibal 2015), it was shown that the compressibility models used to determine the data in Figure 4-22 were faulty; the contribution of resin pressure to the load on the Instron was not accounted for when calculating the compaction pressure on the reinforcement.

In this study, the two compressibility models (from squeeze-flow and directly from the DIC/DAQ data during infusion) were evaluated against each other by plugging each model into the Modi-Correia model and comparing the resultant pressure gradients. Figure 4-21 shows the modeled pressure gradients from the data and compressibility models for the third carbon DIC infusion. Again, the linear Darcy's law gradient, the Modi-Correiea model, and the model coupled with an approximated $P_{cap}$ are all shown. The actual measured resin pressures from the pressure transducers are also included in the graph, arranged similar to Figure 4-22 where the resin pressure across the filled regime is presented in different symbols, for when the flow front is at various lengths corresponding to the position of the 6 pressure transducers. When the flow front is at 20mm, there is only one pressure sensor (the one at 20 mm) measuring pressure at an infused location, resulting in only one data point. When the flow front reaches 200 mm, all 6 sensors are measuring pressure at filled locations and more data points are shown.

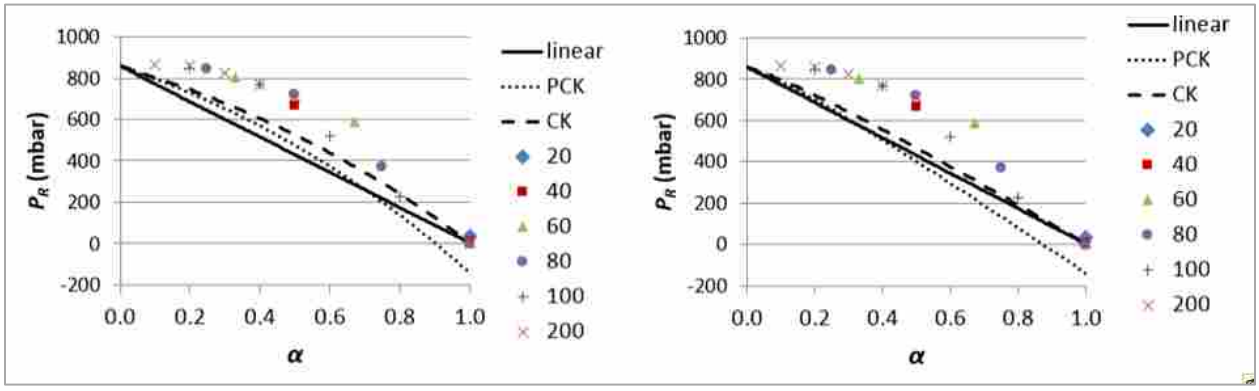


**Figure 4-21: Experimental and Simulated Resin Pressure Gradient from Inlet to Flow Front for Carbon-3 DIC Infusion**

As seen in Figure 4-21, the measured values of $P_R$ "bow" up from the linear Darcy's Law model, as predicted by the Modi-Correia model. But neither compressibility model results in the same amount of curvature as the measured values for $P_R$, which are independent of $P_{cap}$. This

implies that these compressibility models are under-predicting the compliance (opposite of stiffness) due to $P_{cap}$ effects. As discussed in Section 4.2.2, the squeeze-flow tests should have less $P_{cap}$ involved then in the actual infusion. As the left graph represents the filling prediction using the squeeze-flow compressibility model, it exhibits more compliance than the right graph's results based on infusion compressibility. This implies that when $P_{cap}$ forces are involved in the compressibility testing, and not accounted for, i.e. separated from the other pressures involved, then the compressibility results in a lower compliance (stiffer model) than the true nature of the reinforcement. But even the squeeze-flow compressibility model still under predicts the compliance, suggesting that $P_{cap}$ forces may still be somehow involved in that test, although to a lesser extent than during infusion.

As the pressure gradient predictions in the right graph in Figure 4-21 are resultant from compressibility based on full $P_{cap}$ effects, and the measured $P_R$ points are independent of $P_{cap}$, the difference between the two may be an approximation of the relative effect of $P_{cap}$ on the flow rate during infusion. The flow rate is proportional to the pressure gradient at the flow front ($\alpha$ = 0). The predicted pressure gradient with no coupled effects from $P_{cap}$ ends up at $\alpha = 0$ at the same pressure as the measured pressure gradient (the vacuum pressure, 300 Pa), but seems to have a slightly lower pressure gradient (less downward curvature), thus under-predicting the flow rate. The flow model coupled with a $P_{cap}$ term in the pressure balance (dotted line in Figure 4-21) has a slightly steeper pressure gradient than the non-coupled model, and may be closer to the experimental gradient at the flow-front, although it's hard to tell without more data points around the flow front and just behind it. But the difference between the experimental $P_R$ and the coupled model at the flow-front is equal to the approximated value for $P_{cap}$ used in the flow model, which is based on Equation 4-12. Thus the difference is still simulated and not measured.

## 4.3 $P_{cap}$ Comparison Between Dip Tests and DIC/DAQ Testing

Figure 4-22 shows the data from Figure 4-21 (left side – squeeze flow compressibility model), with only experimental data for the pressure gradient when the flow-front is at the transducer at 100 mm. Added to this graph is the "inferred" pressure gradient as was done in Figure 4-22, where the thickness data across the entire 100 mm (sampled at high resolution in DIC) was converted to their equivalent $P_R$ values by using the compressibility model determined from infusion – in essence using the average relationship between DIC data and DAQ data for that test. This allows one to see the entire $P_R$ gradient from the experiment instead of just a couple points at the transducer locations. But as seen in Figure 4-22, this profile departs from the experimental $P_R$ gradient. First, a "tail" is seen in the bottom right, where the inferred $P_R$ values jumps up. This was noted previously (George 2011) and is the effect of measuring thicknesses around the flow front where the reinforcement is only partially saturated, before either bulk flow or $P_{cap}$ effects finish saturating everything just behind the flow front. Partial saturation means the reinforcement is partially dry, which makes the material stiffer due to less lubrication. The length of this tail is thus related to the difference in speeds for capillary flow and bulk flow between the fiber bundles. The compressibility model determination doesn't reflect this partial saturation because most of the transducer data sampling is done when the flow front is somewhere in between the transducers, and very few data comes from when the partially saturated flow front is right over a transducer.

The other departure from the experimental pressure gradient is the drop below the experimental values, even to negative pressures before the partial lubrication tail brings it back up. Although this is not as severe a drop as was seen in Figure 4-22 with a faulty compressibility model, this is still evidence of negative effective pressures due to $P_{cap}$ forces acting on the

pressures involved during infusion. The thickness under the vacuum bag is affected by both $P_R$ and $P_{cap}$, thus the difference between this inferred profile and the $P_R$ experimental values is assumed to be a relative experimental determination of the effects of $P_{cap}$. The precision of DIC testing seems somewhat inadequate to measure the difference between this and the experimental $P_R$ values with confidence (the negative $P_R$ values seem suspiciously low), especially not knowing for sure at what point partial saturation is making the curve shoot up into unusable data. But a difference of about 50 mbar (5 kPa) is a visually approximated difference between the 2 curves. The thickness of the sample by the flow front during this infusion was about 2.2 mm, and this carbon infusion was done in the warp direction. Looking back at Figure 4-14, the warp $P_{cap}$ at this thickness (corresponding to 60% fiber content) was determined in the dip tests to be about 1.3 kPa, which is lower than the 5 kPa estimated from infusions, but is at least in the same order of magnitude, and doesn't look as bad of a match when considering all the sources of error from DIC, DAQ, and compressibility fitting associated with the infusion $P_{cap}$ measurement method. Perhaps with better data sampling, and continued further testing, the relationship between $P_{cap}$ values determined in infusion and in dip testing will be made clearer.

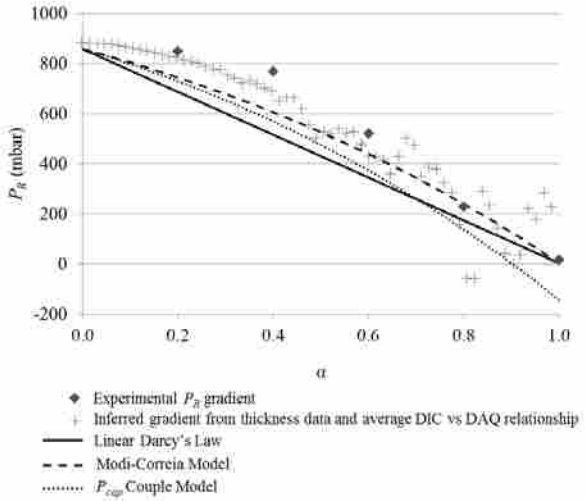


**Figure 4-22: Experimental and Simulated Data of $P_R$ gradient**

# 5 CONCLUSIONS

Fabric dip tests were conducted similar to previous studies, using fluorescent dye to visually track and measure capillary flow. The stitching fibers in a carbon NCF allowed enough light transmission to indicate rise of the flow front. Three methods were used to infer the capillary pressure from the height vs. time data measured in the dip tests: neglecting gravity, partially accounting for gravity, and fully accounting for gravity. The latter method resulted in the highest calculated values of capillary pressures, and is assumed to be the most accurate of the measurement methods, although it was not as precise as the other methods. Values for $P_{cap}$ were measured by this method of ~2 kPa for the carbon fabric. Thus the relative effects of $P_{cap}$ may become significant in flow modeling under certain slow flow conditions in composites processing.

Along with the dip tests, infusions were also monitored by a DIC/DAQ system. Comparison of compressibility data from this experiment with the data from a squeeze-flow test lends evidence to the suspicion that the expansion squeeze-flow data may be resulting in overly low compaction pressures. Squeeze flow testing shows a more constant stiffness, while the infusion testing shows a faster stiffening and ends up at higher compaction pressures required for any $v_F$ higher than about 0.585.

The measured values of resin pressure in these infusion tests "bow" up from the linear Darcy's Law model, as predicted by the Modi-Correia model. The compressibility models used

results in less curvature than the measured values for resin pressure, which are independent of $P_{cap}$. This implies that these compressibility models are under-predicting the compliance (opposite of stiffness) due to $P_{cap}$ effects, which are involved in compressibility testing. The flow model coupled with a $P_{cap}$ term in the pressure balance has a slightly steeper pressure gradient than the non-coupled model, and seems to be closer to the experimental gradient at the flow-front. The dip in the effective resin pressure (inferred from the thickness) to levels below the vacuum pressure can be attributed to $P_{cap}$ and this same dip is seen in the model.

## 5.1 Future Recommendations

For the improvement of future testing and analysis similar to that which has been performed in this work, the following recommendations are given. Dip tests would be repeated, but performed with different fluids to see if the change in contact angle and surface tension does indeed alter the capillary pressure as predicted by Equation 4-12. Each fluid would also be tested to measure the dynamic contact angle $\theta_{CD}$, to improve the resulting $P_{cap}$ in equation 4-12.

# REFERENCES


Ahn, K. J., J. C. Seferis, and J. C. Berg. "Simultaneous measurements of permeability and capillary pressure of thermosetting matrices in woven fabric reinforcements." *Polymer composites* 12.3 (1991): 146-152.

Amico, S.C. *Permeability and Capillary Pressure in the Infiltration of Fibrous Porous Media in Resin Transfer Moulding.* University of Surrey, 2000

Argüelles, P., et al. "European Aeronautics: A vision for 2020." *Advisory Council for Aeronautics Research in Europe, Report* (2001).

Batch, G. L., Y.T. Chen, and C.W. Macoskot. "Capillary impregnation of aligned fibrous beds: experiments and model." *Journal of reinforced plastics and composites* 15.10 (1996): 1027-1051.

"Boeing 787 Dreamliner Specs." *Modern Airliners*. Web. 20 Nov. 2015.

Chang, C.Y., L.W. Hourng, and C.J.Wu. "Numerical study on the capillary effect of resin transfer molding." *Journal of reinforced plastics and composites* 16.6 (1997): 566-586.

Correia, N.A.C.M. Analysis of the vacuum infusion moulding process. PhD. diss. University of Nottingham, 2004.

Darcy, H.P.G. *Les fontaines publiques de la ville deDijon.* Paris: Dalmont (1856).

George, A., H. Ahlborn, M. ElGhareeb, K. Drechsler, and D. Heider. "Compressibility Modeling and Validation for Coupled Flow Simulation." Paper presented at the 18th International Conference on Composite Materials (ICCM), Jeju, South Korea, 2011.

George, A. *Optimization of resin infusion processing for composite materials: simulation and characterization strategies*. Diss. University of Stuttgart, 2011.

George, A. "Rigid Tooling for Optical 3D Wetting Permeability Measurements" FPCM 12 Enschede, The Netherlands. 14 July 2014. Lecture.

Gourichon, B., C. Binetruy, and P. Krawczak. "A new numerical procedure to predict dynamic void content in liquid composite molding." *Composites Part A: applied science and manufacturing* 37.11 (2006): 1961-1969.

Hannibal, P. "Compressibility Measurement and Modeling to Optimize Flow Simulation of Vacuum Infusion Processing for Composite Materials." (2015).

Hattabi, M., et al. "Flow analysis during on-line and radial injection applications in permeability measurements." *Journal of reinforced plastics and composites*24.18 (2005): 1909-1920.

"ImageJ." *ImageJ*. Web. 20 Nov. 2015.

"Innovative Materials | Airbus, a Leading Aircraft Manufacturer."*Airbus*. Web. 20 Nov. 2015.

Kang, M. K., W.I. Lee, and H.T. Hahn. "Formation of microvoids during resin-transfer molding process." *Composites Science and Technology*60.12 (2000): 2427-2434.

Kuentzer, N., et al. "Correlation of void distribution to VARTM manufacturing techniques." *Composites Part A: applied science and manufacturing* 38.3 (2007): 802-813.

Lai, Y.H, B. Khomami, and J.L. Kardos. "Accurate permeability characterization of preforms used in polymer matrix composite fabrication processes." *Polymer Composites* 18.3 (1997): 368-377.

LeBel, F., et al. "Prediction of optimal flow front velocity to minimize void formation in dual scale fibrous reinforcements." *International journal of material forming* 7.1 (2014): 93-116.

Lee, W.J., Characterizing High Performance Composite Processability With Dynamic *Polymer Composites* 9(1) (1988): 36-41.

Lee, Y.N, and S.N. Chiao. "Visualization of dynamic contact angles on cylinder and fiber." *Journal of colloid and interface science* 181.2 (1996): 378-384.

Li, M., et al. "Dynamic capillary impact on longitudinal micro-flow in vacuum assisted impregnation and the unsaturated permeability of inner fiber tows."*Composites Science and Technology* 70.11 (2010): 1628-1636.

Modi, D.G., A. *Modelling and Active Control of the Vacuum Infusion Process for Composites Manufacture* Diss. University of Nottingham, 2008.

Neacsu, V., A. Abu-s a bank of aligned micro-cylinders*International Journal of Multiphase Flow* 32 (2006): 677 691.

Patel, N., and L.J Lee. "Modeling of void formation and removal in liquid composite molding. Part I: Wettability analysis." *Polymer Composites* 17.1 (1996): 96-103.

Pillai, K. M., and S. G. Advani. "A model for unsaturated flow in woven fiber preforms during mold filling in resin transfer molding." *Journal of Composite Materials* 32.19 (1998): 1753-1783.

Ruiz, E., et al. "Optimization of injection flow rate to minimize micro/macro-voids formation in resin transfer molded composites." *Composites science and technology* 66.3 (2006): 475-486.

Simacek, P., V. Neacsu, and S.G. Advani. "A phenomenological model for fiber tow saturation of dual scale fabrics in liquid composite molding."*Polymer Composites* 31.11 (2010): 1881-1889.

Slade, J., K. M. Pillai, and S. G. Advani. "Investigation of unsaturated flow in woven, braided and stitched fiber mats during mold-filling in resin transfer molding." *Polymer Composites* 22.4 (2001): 491.

Vernet, N., et al. "Experimental determination of the permeability of engineering textiles: Benchmark II." *Composites Part A: Applied Science and Manufacturing*61 (2014): 172-184.